Geochimica et Cosmochimica Acta 364 (2024) 129–147

Contents lists available at ScienceDirect

Geochimica et Cosmochimica Acta

journal homepage: www.elsevier.com/locate/gca

The effect of composition, temperature and pressure on the oxidation state and coordination environment of copper in silicate melts

Laura A. Miller [a,*], Andrew J. Berry [a], Hugh St.C. O'Neill [a,b], Jeremy Wykes [c], Matt Newville [d], Tony Lanzirotti [d]

[a] Research School of Earth Sciences, Australian National University, Canberra, ACT 2601, Australia
[b] School of Earth, Atmosphere and Environment, Monash University, Clayton, VIC 3800, Australia
[c] Australian Synchrotron, 800 Blackburn Road, Clayton, VIC 3168, Australia
[d] Center for Advanced Radiation Sources, University of Chicago, Chicago, IL 60637, USA

ARTICLE INFO

Associate editor: Sung Keun Lee

Keywords:
Copper
Oxidation state
XANES spectroscopy
Silicate melts
Oxygen fugacity

ABSTRACT

Copper is a redox variable element that may occur as Cu^0, Cu^+, and Cu^{2+} in the Earth's crust. The oxidation state will affect its partitioning between coexisting minerals, melts and fluids and hence its behaviour in magmatic processes. Copper bearing silicate glasses were quenched from melts with 23 synthetic compositions (19 CaO-Na_2O-MgO-Al_2O_3-SiO_2 (CNMAS), two "granites" containing $K_2O \pm H_2O$, and Fe-bearing "MORB" and "andesite") equilibrated at oxygen fugacities (fO_2), expressed in log units relative to the fayalite-magnetite-quartz (FMQ) buffer, ranging from −0.7 to 14, temperatures from 900 to 1500 °C and pressures from 0 to 2.5 GPa. Cu *K*-edge X-ray absorption near edge structure (XANES) spectra were recorded from the glasses and a pre-edge feature in the XANES spectra was found to scale with the proportion of Cu^+. $Cu^+/\Sigma Cu$ (where $\Sigma Cu = Cu^+ + Cu^{2+}$) was quantified by fitting the intensity of the pre-edge feature as a function of fO_2 to the thermodynamically expected relationship. $Cu^+/\Sigma Cu$ was found to only weakly depend on melt composition, with more basic melts (e.g., basalts rather than granites) preferentially stabilising Cu^{2+}. Increasing temperature stabilises Cu^+, while increasing pressure had little effect on $Cu^+/\Sigma Cu$ in CNMAS melts but preferentially stabilised Cu^{2+} in granite melts. $Cu^+/\Sigma Cu$ can be predicted in silicate melts by the empirical equation:

$$\log(Cu^{2+}/Cu^+) = 0.25(\Delta FMQ + 8.58 - 25050/T + 940P/T - 0.02P) - 4.73 + 5400/T + 1.99\Lambda + (280P - 90P^2)$$

where T is temperature in K, P is pressure in GPa and Λ is the optical basicity of the composition. The effects of fO_2, melt composition, temperature and pressure on $Cu^+/\Sigma Cu$ indicate that Cu^+ will be the dominant oxidation state in terrestrial silicate melts (e.g., $Cu^+/\Sigma Cu$ = 99% in an andesitic melt at 900 °C, 1 GPa and ΔFMQ = 1). The electron exchange reaction $Cu^{2+} + Fe^{2+} \rightarrow Cu^+ + Fe^{3+}$ occurs on cooling and, given the abundance of Fe in natural melts, the oxidation state of Cu in natural glasses is unlikely to correspond to that in the original melt.

1. Introduction

Copper is predicted to be one of the most critical raw materials of the 21st century because of its role in enabling green technologies and doubt as to whether known reserves can meet the expected demand (Tabelin et al., 2021). The vast majority of known Cu deposits are associated with igneous rocks and guidance in the search for new deposits requires a better understanding of the geochemical processes that transport Cu from the deep Earth and concentrate it in economic deposits. Copper is a redox variable element that can occur as Cu^0, Cu^+ and Cu^{2+}. The different oxidations states of Cu have different siderophile (e.g., Righter and Drake, 2000; Righter et al., 2010), chalcophile (e.g., Li and Audetat, 2012; 2015; Kiseeva and Wood, 2013; 2015) and magmaphile (e.g., Liu et al., 2014) affinities, solubilities (e.g., Ripley and Brophy, 1995; Holzheid and Lodders, 2001), and volatilities (e.g., Sossi et al., 2019). Thus, Cu speciation plays an important role in controlling the Cu content of a silicate melt and the partitioning of Cu between different phases (e.g., melt, crystals, sulphide and fluid).

* Corresponding author.
E-mail address: Laura.Miller@anu.edu.au (L.A. Miller).

https://doi.org/10.1016/j.gca.2023.07.021
Received 26 February 2023; Accepted 29 July 2023
Available online 10 August 2023

Previous work has indicated that Cu is likely to occur mainly as Cu^{+} in magmatic silicate melts (e.g., Ripley and Brophy, 1995; Holzheid and Lodders, 2001) and the fluids that exsolve from these melts (e.g., Berry et al., 2009). However, many Cu ore deposits are associated with highly oxidised magmas that may stabilise Cu^{2+} (Richards, 2015). The major controls on the oxidation state of an element in silicate melts are oxygen fugacity (fO_2; e.g., Schreiber, 1987; Berry and O'Neill, 2004; Mare et al., 2020), melt composition (e.g., Berry et al., 2006a; Burnham and Berry, 2014; Burnham et al., 2015; Miller et al., 2019), temperature (e.g., Kress and Carmichael, 1991; Burnham and Berry, 2014; Burnham et al., 2015) and pressure (e.g., Kress and Carmichael, 1991; O'Neill et al., 2006; Matjuschkin et al., 2016; Berry et al., 2021). The effect of melt composition can be attributed to melt structure, usually parameterised by NBO/T (non-bridging oxygens/tetrahedrally coordinated cations; Mysen et al., 1982; Mills, 1993; Nesbitt et al., 2020), or melt chemistry, parameterised by optical basicity (Λ; Duffy, 1993; Lebouteiller and Courtine, 1998), where more basic melts generally stabilise higher charged cations. At constant values of fO_2, referenced to the conventional standard state of O_2 as an ideal gas, lower temperatures stabilise cations with higher charges (e.g., Kress and Carmichael, 1991; Burnham and Berry, 2014; Burnham et al., 2015), while lower pressures stabilise the cation with the oxide component that has the larger molar volume (O'Neill et al., 2006).

The oxidation state and coordination environment of Cu can be determined from Cu *K*-edge X-ray absorption near edge structure (XANES) spectra (e.g., Kau et al., 1987; Maurizio et al., 2000; Fulton et al., 2000; Berry et al., 2009; Rudolph and Jacob, 2018). These studies have found that Cu^{+} forms linear, trigonal planar and tetrahedral complexes while Cu^{2+} generally forms tetragonally-distorted octahedral complexes. Cu^{+} can be identified in *K*-edge XANES spectra by the presence of an intense pre-edge peak between 8983 and 8986 eV (Kau et al., 1987). For Cu^{+} the unoccupied electron orbitals with the lowest energy are the 4*p* and the pre-edge peak is attributed to a $1s \rightarrow 4p$ transition. The intensity and energy of this peak correlates with the coordination of Cu^{+} (see Fig. 2 in Kau et al., 1987), where the intensity of the peak decreases as the coordination number increases due to mixing of the 4*p* and ligand orbitals. A low intensity peak at ~8979 eV is observed in all Cu^{2+} complexes and corresponds to the dipole forbidden $1s \rightarrow 3d$ transition, which cannot occur for Cu^{+} as the 3*d* shell is full (Kau et al., 1987; Fulton et al., 2000). The d^9 configuration of Cu^{2+} results in a Jahn-Teller distortion (i.e., a geometric distortion that reduces the symmetry and energy of a coordination complex). This distortion is characterised by a shoulder (8983–8985 eV) on the main absorption edge, where the energy separation of this shoulder from the edge is related to the degree of distortion from octahedral (e.g., Palladino et al., 1993). The energy of the shoulder has also been observed to change with the coordinating ligands (decreasing with increasing covalency of the equatorial ligands; Kau et al., 1987). The shoulder has been variously interpreted as a 'shakedown', in which a Cu^{2+} $1s \rightarrow 4p$ transition occurs simultaneously with a ligand-to-metal charge transfer (Blair and Goddard, 1980), a $1s \rightarrow 4p_z$ bound-to-bound state transition (Smith et al., 1985), and multiple scattering from the axial ligands (Onori et al., 1988). The shoulder cannot be easily resolved for distortions less than 0.3–0.4 Å and is more readily observed in the derivative spectrum, where the components are commonly referred to as the α and β peaks (e.g., Palladino et al., 1993; Alcacio et al., 2001; Berry et al., 2009).

Here we use XANES spectroscopy to determine $Cu^{+}/\Sigma Cu$, where $\Sigma Cu = Cu^{+} + Cu^{2+}$, for silicate glasses quenched from melts of a range of compositions equilibrated as a function of fO_2 (0.7 to 14 in log units relative to the fayalite-magnetite-quartz, FMQ, buffer), temperature (900–1500 °C) and pressure (ambient to 2.5 GPa). Oxygen fugacities in this study are reported relative to both the conventional standard state (O_2 as an ideal gas at 1 bar and the temperature of interest) and FMQ. The FMQ standard state is convenient for discussing redox speciation in silicate melts because at constant ΔFMQ changes in speciation with temperature tend to be small (O'Neill et al., 2018).

2. Experimental

A number of compositions (n = 19) in the system $CaO\text{-}Na_2O\text{-}MgO\text{-}Al_2O_3\text{-}SiO_2$ (CNMAS) were selected to investigate the effect of melt structure and composition on the oxidation state of Cu. The compositions were chosen so that a wide range of major element oxide contents, and as a consequence compositional and structural parameters, were covered, in addition to having low liquidus temperatures to minimise Cu loss by volatility at atmospheric pressure. Synthetic mid-ocean-ridge-basalt (MORB) and andesite compositions were used to investigate the effect of Fe. The compositions are given in Table 1 and are described in more detail in O'Neill and Eggins (2002) and O'Neill and Berry (2006). The effect of temperature on $Cu^{+}/\Sigma Cu$ was investigated at atmospheric pressure using CMAS7G and at 1 GPa using a hydrous (10 wt% H_2O) K_2O-bearing granite (more correctly termed a haplogranite but called a granite here for bevity; Holtz et al., 1992; Table 1). The effect of pressure on $Cu^{+}/\Sigma Cu$ at 1400 °C was investigated using CMAS7G and a K_2O-bearing anhydrous granite composition, where the latter is the anhydrous equivalent of the hydrous granite. The CMAS, hydrous granite and granite compositions were selected due to their low melting temperatures and hence ability to produce crystal-free glasses in experiments at low-temperatures and high-pressures. Further, the CMAS7G composition is structurally similar to MORB.

The compositions were prepared using reagent grade oxide and carbonate powders that were mixed under acetone for a minimum of 20 min. using an agate pestle and mortar. SiO_2, Al_2O_3 and MgO were dried at 1000 °C, $CaCO_3$ and TiO_2 at 400 °C, and Na_2CO_3, K_2CO_3 and Fe_2O_3 at 300 °C prior to weighing. The mixes were pressed into pellets, decarbonated at 1000 °C for 12 h and reground. Copper was added as a solution (1000 μg/ml) prepared by dissolving copper nitrate trihydrate in acetone, which, on evaporation, gave homogenously distributed Cu with concentrations that could be easily varied.

A gas mixing vertical tube furnace was used to synthesise glasses as a function of fO_2, temperature and time at ambient pressure. The samples could not be held on metal loops, which are conventionally used for experiments of this type (e.g., Berry et al., 2006a) due to the propensity of Cu to alloy with other metals, and instead the melts were contained in wells drilled in dense high-purity (99.99%) alumina disks. The disks contained eight wells, each of 5 mm diameter. The arrangement is similar to the graphite holders described in O'Neill and Berry (2006) and an example is shown in Fig. S1. The following gas mixes were used to impose $\log fO_2$s at 1300 °C: O_2 (0; ΔFMQ = 7.3), CO_2/O_2 (from −1 to −3; ΔFMQ = 6.3 to 4.3) and CO/CO_2 (from −4 to −8; ΔFMQ = 3.3 to 1.3). Redox series glasses were prepared by equilibrating CNMAS, MORB and andesite melts containing either 2000 or 7000 ppm Cu over a range of fO_2 (ΔFMQ = 7.3 to 1.3) at 1300 °C for 24 h. The two different Cu concentrations were due to concern about the volatility of Cu. Sodium is volatile under reducing conditions (O'Neill, 2005) and hence Na-bearing glasses were only prepared at $\log fO_2 > -4$ (ΔFMQ > 3.3). A disk containing eight samples was equilibrated for 72 h at 1300 °C and ΔFMQ = 7.3 to investigate the dissolution of Al_2O_3 from the holder into the melt and the loss of Cu by volatility. A temperature series was prepared by equilibrating CMAS7G at 1200–1500 °C and $\log fO_2 = 0$ (ΔFMQ = 8.3 to 5.3) for 24 h. Melts were quenched in water to give glasses. After the experiments the alumina disks were impregnated with an epoxy resin, ground using diamond grit wheels and polished using diamond grit laps.

Piston-cylinder apparatus were used to synthesise glasses at pressures ≥ 0.5 GPa. The metal–metal oxide buffers Pt-PtO_2 (ΔFMQ = 11; Belonoshko and Saxena, 1991), Ir-IrO_2 (ΔFMQ = 8; O'Neill and Nell, 1997), Ru-RuO_2 (ΔFMQ = 5; O'Neill and Nell, 1997) and Re-ReO_2 (ΔFMQ = 2.5; Pownceby and O'Neill, 1994) were used to control the fO_2 of these experiments (the ΔFMQ quoted here are for 1 GPa and 1400 °C; see Table 3). Pt capsules were used such that only PtO_2 needed to be added to samples equilibrated with the Pt-PtO_2 buffer. At temperatures ≥ 1400 °C PtO_2 breaks down to give O_2 at a pressure equal to the

Table 1
Glass compositions (wt.%) determined by EDS and normalised to 100, the optical basicity (Λ), and non-bridging oxygens/tetrahedral cations (NBO/T). The uncertainty for each oxide is ~0.2 (determined from replicate analyses). The average uncertainties of Λ and NBO/T are 0.001 and 0.010, respectively.

Composition	SiO_2	Al_2O_3	MgO	CaO	FeO*	TiO_2	Na_2O	K_2O	H_2O**	Λ	NBO/T
AnDi	48.6	17.5	10.7	23.2	–	–	–	–	–	0.607	0.884
CMAS7G	59.5	13.8	2.5	24.2	–	–	–	–	–	0.581	0.567
Longhi2	48.0	16.0	5.5	30.5	–	–	–	–	–	0.618	0.937
Longhi3	62.7	18.1	9.2	10.0	–	–	–	–	–	0.554	0.328
Longhi4	62.4	15.5	5.3	16.8	–	–	–	–	–	0.564	0.416
Osborn1	42.3	21.0	7.9	28.8	–	–	–	–	–	0.626	0.903
Osborn3	47.1	17.9	13.4	21.6	–	–	–	–	–	0.609	0.951
Osborn4	44.2	18.9	10.7	26.2	–	–	–	–	–	0.621	0.989
Osborn5	42.1	21.5	8.8	27.6	–	–	–	–	–	0.625	0.890
Osborn6	49.5	21.3	14.9	14.3	–	–	–	–	–	0.590	0.669
CAS1	40.8	21.4	–	37.8	–	–	–	–	–	0.640	0.846
CAS4	51.9	15.9	–	32.2	–	–	–	–	–	0.608	0.713
CAS5	61.7	15.8	–	22.5	–	–	–	–	–	0.571	0.369
Na1	52.4	18.7	2.3	21.3	–	–	5.3	–	–	0.600	0.547
Na2	44.4	23.5	0.3	26.2	–	–	5.6	–	–	0.622	0.557
Na3	42.1	23.6	4.1	24.0	–	–	6.2	–	–	0.628	0.686
Na4	58.0	18.9	8.4	8.6	–	–	6.1	–	–	0.573	0.411
Na5	55.2	15.9	8.8	15.1	–	–	5.0	–	–	0.590	0.670
Na6	40.5	22.8	7.4	23.0	–	–	6.3	–	–	0.634	0.843
Granite	79.3	14.4	–	–	–	–	3.0	3.3	–	0.517	−0.072
Hydrous granite	69.5	12.4	–	–	–	–	4.2	3.9	10	0.505	0.787
MORB	52.1	17.8	8.2	12.1	9.7	0.1	–	–	–	0.586	0.620
Andesite	61.6	19.8	2.3	7.7	3.1	0.1	1.1	4.3	–	0.560	0.151

– < 0.2.
* All Fe was assumed to be Fe^{2+} for the calculation of Λ and NBO/T.
** Nominal value.

confining pressure, which sets the fO_2 (Berry et al., 2003a). The Ir-IrO_2 and Ru-RuO_2 buffers were prepared with 20% metal and 80% oxide, while Re-ReO_2 was prepared with 30% metal and 70% oxide. The buffers were placed as layers at the top and bottom of the capsules other than for the hydrous granite temperature series where the buffers were only placed at the bottom. The amounts of PtO_2 and metal–metal oxide mixes were ~20% by mass of the silicate compositions. The highest fO_2 accessible at atmospheric pressure is that of O_2 at 1 bar. To prepare highly oxidised glasses for the redox series, the CNMAS, MORB and andesite compositions were equilibrated at 1400 °C and 1 GPa, in sealed Pt capsules with PtO_2 for 5 h. The hydrous granite samples were prepared by packing the capsules with the fO_2 buffer and the anhydrous granite oxide mix and then adding 10 wt% of deionised water using a syringe. Each capsule was partially submerged in a water bath with only the top exposed while sealed by welding. This was to ensure that the capsule body did not heat up during welding and that the added H_2O was retained. To confirm that water was not lost the capsules were weighed before and after welding. The hydrous granite temperature series was prepared by equilibrating the samples with Pt-PtO_2 and Ir-IrO_2 in sealed Pt capsules at 900, 1100 and 1400 °C and 1 GPa for 5 h. A single sample using a $Cu_{15}Pd_{85}$ capsule was equilibrated at the Cu-Cu_2O buffer (i.e., Cu^0 in the $Cu_{15}Pd_{85}$ capsule and Cu^+ in the silicate melt; ΔFMQ = 6.4; Table 3), 900 °C and 1 GPa for 5 h. The mix added to this capsule did not contain Cu and the $Cu_{15}Pd_{85}$ capsule acted as the source of Cu. Pressure series were prepared by equilibrating CMAS7G containing 5000 ppm Cu, and the hydrous granite composition containing 2000 ppm Cu, with Pt-PtO_2, Ir-IrO_2, Ru-RuO_2 and Re-ReO_2 in sealed Pt capsules at 0.5, 1.0, 2.0 and 2.5 GPa and 1400 °C for 5 h. All piston cylinder experiments used a graphite heater, a pyrex and Na-Cl pressure medium, and MgO machined to contain the Pt capsules. Up to three capsules (e.g., each with a different fO_2 buffer) could be placed within the MgO and equilibrated simultaneously. After the experiment, the capsules were mounted in epoxy resin, ground to expose the sample and polished.

$Cu(NO_3)_2{\cdot}3H_2O$, $CuSO_4{\cdot}5H_2O$, CuO and Cu_2O were used as XANES standards. The phase purity of each compound was confirmed by X-ray diffraction. The standards were mixed with microcrystalline cellulose under ethanol except for $Cu(NO_3)_2{\cdot}3H_2O$, which was mixed with boron nitride, to give powders with 3000 ppm Cu. The powders were then pressed into 10 mm diameter pellets.

3. Analytical

The glasses were examined using a JEOL 6400 scanning electron microscope (SEM) operating at 15 kv. Back-scattered electron (BSE) images were obtained to check for the presence of crystals. Energy dispersive spectroscopy (EDS) was used to identify any crystals and determine the major element composition and homogeneity of the glasses. The compositions of a sub-set of samples were determined by wavelength dispersive spectroscopy (WDS) using a JEOL JXA-8530F electron probe microanalyser (EPMA) operating at 15 kV and 20 nA.

The concentrations of ^{65}Cu, ^{101}Ru, ^{185}Re, ^{193}Ir and ^{195}Pt in the glasses were determined by laser ablation inductively coupled plasma mass spectrometry (LA-ICPMS). The instrument comprises a 193 nm ArF EXCIMER laser coupled to an Agilent 7500S quadrupole ICP-MS. The diameter of the analysis spot was 105 μm. The acquisition time per analysis was 60 s, with the first and last 10 s recorded as background before and after ablation. NIST 610 was used as the external standard, and NIST 612 and BCR-2G as secondary standards, for ^{65}Cu and ^{195}Pt. GM-01 (Chen et al., 2020) was used as the external standard, and NIST 612 and NIST 610 as secondary standards, for ^{101}Ru, ^{185}Re, ^{193}Ir and ^{195}Pt. The Si content of each glass determined by EDS was used as the internal standard. Glass analyses were obtained in batches of up to 10, bracketed before and after by analyses of the standards. The program Iolite (Paton et al., 2011) was used for data reduction. The precision of the LA-ICPMS data was determined from replicate analyses of the standards to be approximately 5%.

The H_2O contents of the hydrous granite glasses were qualitatively determined using Raman spectroscopy. Raman spectra were recorded using a T64000 Jobin-Yvon Raman triple spectrometer equipped with a nitrogen cooled 1024 CCD detector, a 2400 line/mm grating and confocal system. Samples were excited using a 532 nm laser focused on the surface using a 100x Olympus objective. The spatial resolution was determined by the objective and was <1 μm. The spectral resolution was determined by the grating and was ~1.2 cm^{-1}. Spectra were recorded from 50 to 4000 cm^{-1}. The spectra were normalised following Le Losq et al. (2012).

Due to the limited availability of synchrotron beamtime, some spectra were recorded at the X-ray absorption spectroscopy (XAS) beamline of the Australian Synchrotron (AS) and others at 13-ID-E (GSECARS) of the Advanced Photon Source (APS). As beam-induced changes (i.e., beam damage) were found to affect samples equilibrated at pressures ≥ 0.5 GPa more so than samples equilibrated at atmospheric pressure (see Results), and as it was easier to mitigate beam damage at the APS, spectra were recorded for the one atmosphere samples at the AS and for the high pressure samples at the APS. Spectra were recoded for a subset of glasses (CMAS7G, AnDi, CAS1, CAS4, Longhi2 and Longhi 3 redox series) at both beamlines to enable integration of the two datasets.

At the AS the excitation energy was selected using a Si(1 1 1) double crystal monochromator. High-energy harmonics were rejected using a Rh stripe on the focusing mirror. The energy was calibrated by defining the first peak in the derivative spectrum of Cu foil, recorded in transmission, to be at 8980.48 (Kraft et al., 1996). The energy resolution at the Cu *K*-edge (including the core–hole width) was 2.06 eV. Spectra were recorded from Cu foil at intervals throughout the beam time. Fluorescence was recorded using a 100 element Ge detector. The distance between each sample and the detector was adjusted to maintain a constant count rate that was within the linear range of the signal processing electronics. For spectra recorded from Fe-bearing glasses the beam size on the sample was 3 mm (horizontal) by 2 mm (vertical) and Al foil was placed in front of the detector to reduce the fluorescence from Fe relative to that from Cu. For all other samples, the beam size was 350 μm (horizontal) by 250 μm (vertical). The sample chamber was filled with He to reduce attenuation and scatter. Spectra were recorded from 8800 to 9360 eV with a step size of 5 eV up to 8960 eV, 0.2 eV between 8960 and 9010 eV, 0.5 eV between 9010 and 9060 eV, and 10 eV above 9060 eV. The count time was 2 s per point giving a total acquisition time of ~21 min. The signals from the 100 detector elements were averaged and the resulting spectra were normalised using ATHENA (Ravel and Newville, 2005).

At the APS the excitation energy was also selected using a Si(1 1 1) double crystal monochromator. The beam was focussed using Kirkpatrick-Baez mirrors, which were also used to reject high energy harmonics. The energy resolution (including the core–hole width) was 1.83 eV. Fluorescence was recorded using a four-element Vortex ME-4 silicon drift detector. The distance between each sample and the detector was adjusted to maintain a constant count rate. To minimise beam damage the beam was attenuated using Al foil and defocused. The resultant spot size on the sample was 100 μm. Beam damage was monitored by recording fluorescence as a function of time (~300 s) at the energy of the 1*s*-4*p* peak (~8984 eV). This was not possible at the AS due to the wake-up time of the detector after opening the shutter. To further minimise beam damage spectra were recorded with relatively fast scan parameters; a step size of 4 eV from 8910 to 8970, 0.2 eV from 8970 to 9020, and a *k* step of 0.081 from 9020 eV to $k = 10$. The count time was 0.5 s per point giving a total acquisition time of ~3 min. For every sample the fluorescence as a function of time was recorded followed by six spectra recorded from different positions. The energy was corrected by aligning spectra with those of the same sample recorded at the AS. The spectra were averaged and normalised using ATHENA (Ravel and Newville, 2005).

4. Results

The colour of the Fe-free glasses changed from blue or blue/green under oxidising conditions (ΔFMQ ≥ 5.3) to colourless under reducing conditions (Fig. S1). The Longhi3 glasses had a different colour to the other Fe-free glasses and were green at ΔFMQ = 5.3 and gold from ΔFMQ = 4.3 to −0.7. The MORB glasses varied from black to dark green as the fO_2 decreased.

Starting compositions with a low Al_2O_3 content (<15 wt%; Osborn1, 3 and 4) became enriched in Al_2O_3 (an increase of up to 10 wt%) during the experiments from dissolution of the alumina crucible (e.g., Haughton et al., 1974). The Al contents of these glasses were homogenous suggesting that each melt and crucible had reached equilibrium. As every glass in a redox series was affected in the same way this resulted in a compositionally consistent series, albeit not with the initially desired composition. For many samples, a rim of Al-rich crystals (<150 μm) was observed at the interface of the alumina crucible and glass. This rim was larger (<300 μm wide) in the glasses equilibrated for 72 h, although these glasses had the same (or only slightly, < 1 wt.%, higher) homogenous Al_2O_3 contents as the glasses equilibrated for 24 h. Given the relative size of the glasses (5 mm) and rims (<150 μm) the Al-rich crystals were easily avoided by analysing the centre of the glass (EDS, WDS, LA-ICPMS and XANES). The Osborn6 and hydrous granite glasses were highly vesicular. The reasons for the vesicularity of the Osborn6 glasses are unknown, whereas the hydrous granite glasses are likely to have lost water during quenching producing vesicles. The glass compositions determined by EDS are given in Table 1 and are, within uncertainty, equal to those determined by WDS for the subset of samples for which data were obtained. The Fe contents of the nominally Fe-free glasses were below the detection limit of WDS (50 ppm). Raman spectra recorded for the hydrous granite glasses all have a large OH + H_2O peak (an intense broad band between 3000 and 4000 cm^{-1}; Chabiron et al., 2004; Le Losq et al., 2012), which was qualitatively consistent with ~10 wt% H_2O.

The glasses equilibrated at $\log fO_2 = 0$ for 24 and 72 h retained their starting Cu contents as did those equilibrated in Pt capsules. However, the Cu contents of the redox series glasses decrease with decreasing fO_2, with ~50% Cu lost at $\log fO_2 = -7$. The Cu contents of the glasses are given in Tables 2 and 3. The Pt contents of the glasses equilibrated with PtO_2 range from 3000 to 6000 ppm, which is consistent with the solubility of Pt under oxidising conditions (Ertel et al., 1999). The Ir, Ru and Re contents of the glasses equilibrated with these metals as buffers are <150, <1 and <5 ppm respectively.

4.1. XANES results

Normalised Cu *K*-edge XANES spectra of the standards are shown in Fig. S2. The first peak in the derivative spectrum is at 8980.4, 8981.3 and 8985.2 eV for Cu^0, Cu_2^+O and $Cu^{2+}O$, respectively.

Representative spectra of the CNMAS redox series compositions are shown in Fig. 1a,b and for the remaining CNMAS compositions in Fig. S3 and S4. The spectra shown in Fig. 1a,b and Fig. S3 were recorded at the AS and those in Fig. S4 at the APS. The spectra recorded from samples equilibrated at ΔFMQ ≤ 7.3 all exhibit a pre-edge peak at ~8984 eV (Fig. 1a,b). The intensity of this peak increases with decreasing fO_2 of equilibration. The energy of the peak and the systematic variation its intensity with fO_2 allows it to be assigned to the $1s \rightarrow 4p$ transition of Cu^+ (Kau et al., 1987; Rudolph and Jacob, 2018). A weak peak at ~8979 eV is present in the spectra recorded from the oxidised samples and appears in the derivative at ~8978 eV (black spectra; Fig. 1a,b,e,f). The energy and intensity of this peak is consistent with the $1s \rightarrow 3d$ transition of Cu^{2+} (Kau et al., 1987; Rudolph and Jacob, 2018). A shoulder on the absorption edge of the oxidised samples near ~8988 eV (black spectra; Fig. 1a,b) is clearly defined as a peak (α) in the derivative spectra at ~8986.4 eV (black spectra; Fig. 1e,f) and is attributed to Cu^{2+}. The crest of the main edge at ~8996.4 eV changes from a sharp, rounded peak to a broad, flat peak with increasing fO_2 of equilibration (Fig. 1a,b). This change in shape is attributed to a decreasing proportion of Cu^+ and an increasing proportion of Cu^{2+}. In the derivative the main absorption edge corresponds to a peak (β) at 8992.5 eV (Fig. 1e,f). The spectra of a redox series of a given composition pass through two isosbestic points, at ~8992.5 and ~9007 eV (Fig. 1a,b), indicating that they comprise two components. The features of the spectra and their systematic variation with fO_2 indicate that these two components are Cu^+ and Cu^{2+}. If a glass contained a third species (e.g., Cu^+ or Cu^{2+} in a different coordination environment or Cu^0) then its spectrum would not pass through the isosbestic points defined by the other spectra of the series.

Table 2
The Cu content (ppm), and $I_{1s/4p}$ of Cu *K*-edge XANES spectra recorded at the Australian Synchrotron (Raw) and corrected using Eq. (2) (Cor.), of glasses quenched from melts equilibrated at (i) 1300 °C, atmospheric pressure and various various logfO_2s (0 to −8, or −0.7 to 7.3 relative to fayalite-magnetite-quartz, FMQ) and 1400 °C, 1 GPa and logfO_2 = 4.7 (ΔFMQ = 11; redox series), and (ii) atmospheric pressure, logfO_2 = 0, and various temperatures (1200 to 1500 °C; CMAS7G temperature series) and $Cu^+/\Sigma Cu$ determined from fitting the corrected $I_{1s/4p}$ simultaneously to Eqs. (5), (6), (7) and (8) with melt composition parameterised by NBO/T, optical basicity (Λ) and single cation mole fractions (c_z). The uncertainties associated with $Cu^+/\Sigma Cu$ are <0.01.

Composition	logfO_2 or Temperature	ΔFMQ	Cu	$I_{1s/4p}$		$Cu^+/\Sigma Cu$		
				Raw	Cor.	NBO/T	Λ	C_z
AnDi	4.7(5)	10.6	7800(100)	0.120	0.07(1)	0.00	0.00	0.00
	0.0(3)	7.3	6580(3)	0.566	0.63(2)	0.54	0.56	0.56
	−1.0(3)	6.3	–	0.682	0.78(2)	0.68	0.69	0.69
	−2.0(3)	5.3	–	0.766	0.89(3)	0.79	0.80	0.80
	−3.0(1)	4.3	–	0.863	1.01(3)	0.87	0.88	0.88
	−5.0(3)	2.3	4270(20)	0.909	1.07(3)	0.95	0.96	0.96
	−6.0(3)	1.3	3540(20)	0.838	0.98(3)	0.97	0.98	0.98
CMAS7G	4.7(5)	10.6	7200(100)	0.106	0.10(1)	0.00	0.00	0.00
	0.0(3)	7.3	7060(30)	0.597	0.67(2)	0.58	0.59	0.58
	−1.0(3)	6.3	7070(50)	0.720	0.83(3)	0.71	0.72	0.71
	−2.0(3)	5.3	6700(20)	0.795	0.92(3)	0.81	0.82	0.81
	−3.0(1)	4.3	–	0.961 [a]	1.13(3)	–	–	–
	−5.0(3)	2.3	5880(30)	0.927	1.09(3)	0.96	0.96	0.96
	−6.0(3)	1.3	5240(30)	0.928	1.09(3)	0.98	0.98	0.98
	−7.0(3)	0.3	4810(30)	0.930	1.09(3)	0.99	0.99	0.99
	−8.0(3)	−0.7	2980(10)	0.954	1.12(3)	0.99	0.99	0.99
Longhi2	4.7(5)	10.6	8800(100)	0.126	0.08(1)	0.00	0.00	0.00
	0.0(3)	7.3	7480(8)	0.546	0.61(2)	0.53	0.55	0.54
	−1.0(3)	6.3	5340(20)	0.672	0.77(2)	0.67	0.68	0.67
	−2.0(3)	5.3	5200(2)	0.757	0.87(3)	0.78	0.79	0.79
	−3.0(1)	4.3	–	0.793	0.92(3)	0.87	0.87	0.87
	−5.0(3)	2.3	4330(40)	0.892	1.04(3)	0.95	0.96	0.95
	−6.0(3)	1.3	3410(20)	0.898	1.05(3)	0.97	0.97	0.97
	−7.0(3)	0.3	3000(50)	0.800 [a]	0.93(3)	–	–	–
	−8.0(3)	−0.7	2886(2)	0.495 [a]	0.54(2)	–	–	–
Longhi3	4.7(5)	10.6	6000(60)	0.148	0.11(1)	0.00	0.00	0.00
	0.0(3)	7.3	7220(30)	0.785	0.91(3)	0.60	0.62	0.64
	−1.0(3)	6.3	5330(30)	0.863	1.01(3)	0.73	0.74	0.76
	−2.0(3)	5.3	–	0.925	1.09(3)	0.83	0.84	0.85
	−3.0(1)	4.3	–	0.884 [a]	1.03(3)	–	–	–
	−5.0(3)	2.3	5170(10)	1.013 [a]	1.20(4)	–	–	–
	−6.0(3)	1.3	4630(30)	1.031	1.22(4)	0.98	0.98	0.98
	−7.0(3)	0.3	5050(10)	1.041	1.23(4)	0.99	0.99	0.99
	−8.0(3)	−0.7	4600(30)	1.013 [a]	1.20(4)	–	–	–
Longhi4	4.7(5)	10.6	2000(10)	0.132	0.09(1)	0.00	0.00	0.00
	0.0(3)	7.3	–	0.685	0.78(2)	0.59	0.61	0.61
	−1.0(3)	6.3	2200(2)	0.790	0.92(3)	0.72	0.73	0.74
	−2.0(3)	5.3	2110(20)	0.844	0.98(3)	0.82	0.83	0.83
	−3.0(1)	4.3	2100(10)	0.927	1.09(3)	0.89	0.90	0.90
	−7.0(3)	0.3	1412(6)	0.986	1.16(3)	0.99	0.99	0.99
Osborn1	4.7(5)	10.6	2000(40)	0.125	0.08(1)	0.00	0.00	0.00
	0.0(3)	7.3	2060(6)	0.532	0.59(2)	0.54	0.54	0.54
	−1.0(3)	6.3	2006(4)	0.661	0.75(2)	0.67	0.67	0.68
	−2.0(3)	5.3	1960(5)	0.709	0.81(3)	0.79	0.79	0.79
	−3.0(1)	4.3	1809(3)	0.837	0.97(3)	0.87	0.87	0.87
	−7.0(3)	0.3	800(10)	0.907	1.06(3)	0.98	0.98	0.99
Osborn3	4.7(5)	10.6	2400(100)	0.125	0.08(1)	0.00	0.00	0.00
	0.0(3)	7.3	2150(20)	0.552	0.62(2)	0.53	0.56	0.55
	−1.0(3)	6.3	2216(2)	0.679	0.78(2)	0.67	0.69	0.69
	−2.0(3)	5.3	2133(5)	0.730	0.84(3)	0.78	0.80	0.80
	−3.0(1)	4.3	2037(6)	0.853	0.99(3)	0.86	0.88	0.88
	−7.0(3)	0.3	1071(2)	0.930	1.09(3)	0.98	0.99	0.99
Osborn4	4.7(5)	10.6	2168(9)	0.121	0.07(1)	0.00	0.00	0.00
	0.0(3)	7.3	2220(5)	0.550	0.61(2)	0.53	0.54	0.54
	−1.0(3)	6.3	2180(10)	0.663	0.76(2)	0.66	0.68	0.68
	−2.0(3)	5.3	2094(6)	0.714	0.82(3)	0.78	0.79	0.79
	−3.0(1)	4.3	1948(7)	0.840	0.98(3)	0.86	0.87	0.87
	−7.0(3)	0.3	835(6)	0.909	1.07(3)	0.98	0.99	0.99
Osborn5	4.7(5)	10.6	2100(100)	0.116	0.07(1)	0.00	0.00	0.00
	0.0(3)	7.3	2290(10)	0.540	0.60(2)	0.54	0.54	0.55
	−1.0(3)	6.3	2256(3)	0.666	0.76(2)	0.67	0.68	0.68
	−2.0(3)	5.3	2191(7)	0.720	0.83(3)	0.79	0.79	0.79
	−3.0(1)	4.3	2051(6)	0.842	0.98(3)	0.87	0.87	0.87
	−7.0(3)	0.3	980(20)	0.907	1.06(3)	0.98	0.99	0.99
Osborn6	4.7(5)	10.6	2150(30)	0.125	0.08(1)	0.00	0.00	0.00
	0.0(3)	7.3	–	0.572	0.64(2)	0.56	0.58	0.59
	−1.0(3)	6.3	2180(50)	0.712	0.82(3)	0.70	0.71	0.72
	−2.0(3)	5.3	2090(20)	0.770	0.89(3)	0.80	0.81	0.82

(*continued on next page*)

Table 2 (*continued*)

Composition	logfO_2 or Temperature	ΔFMQ	Cu	$I_{1s/4p}$		$Cu^+/\Sigma Cu$		
				Raw	Cor.	NBO/T	Λ	C_z
	−3.0(1)	4.3	2030(90)	0.872	1.02(3)	0.88	0.89	0.89
	−7.0(3)	0.3	1120(20)	0.882	1.03(3)	0.99	0.99	0.99
CAS1	4.7(5)	10.6	7320(40)	0.125	0.08(1)	0.00	0.00	0.00
	0.0(3)	7.3	6090(8)	0.552	0.62(2)	0.54	0.52	0.53
	−1.0(3)	6.3	5431(6)	0.641	0.73(2)	0.68	0.66	0.66
	−2.0(3)	5.3	5250(20)	0.724	0.83(3)	0.79	0.78	0.78
	−3.0(1)	4.3	–	0.785	0.91(3)	0.87	0.86	0.86
	−5.0(3)	2.3	4110(10)	0.797 [a]	0.92(3)	–	–	–
	−6.0(3)	1.3	2660(10)	0.839	0.98(3)	0.97	0.97	0.97
	−7.0(3)	0.3	2050(20)	0.878	1.03(3)	0.99	0.98	0.98
	−8.0(3)	−0.7	1190(40)	0.885	1.04(3)	0.99	0.99	0.99
CAS4	4.7(5)	10.6	5940(20)	0.125	0.08(1)	0.00	0.00	0.00
	0.0(3)	7.3	7670(2)	0.531	0.59(2)	0.56	0.56	0.55
	0.0(3)	7.3	7670(2)	0.526	0.58(2)	0.56	0.56	0.55
	−1.0(3)	6.3	5610(10)	0.662	0.75(2)	0.69	0.69	0.68
	−2.0(3)	5.3	4830(10)	0.741	0.85(3)	0.80	0.80	0.79
	−3.0(1)	4.3	–	1.006 [a]	1.19(3)	–	–	–
	−5.0(3)	2.3	4680(70)	0.898	1.05(3)	0.96	0.96	0.96
	−6.0(3)	1.3	3216(3)	0.906	1.06(3)	0.98	0.98	0.97
	−7.0(3)	0.3	2470(20)	0.821 [a]	0.95(3)	–	–	–
	−8.0(3)	−0.7	2280(90)	0.867 [a]	1.01(3)	–	–	–
CAS5	4.7(5)	10.6	2030(40)	0.125	0.08(1)	0.00	0.00	0.00
	0.0(3)	7.3	–	0.636	0.72(2)	0.60	0.60	0.60
	−1.0(3)	6.3	2220(5)	0.736	0.85(3)	0.73	0.73	0.73
	−2.0(3)	5.3	2130(10)	0.781	0.90(3)	0.83	0.83	0.83
	−3.0(1)	4.3	2117(9)	0.879	1.03(3)	0.89	0.89	0.90
	−7.0(3)	0.3	1343(7)	0.935	1.10(3)	0.99	0.99	0.99
Na1	4.7(5)	10.6	3600(40)	0.125	0.08(1)	0.00	0.00	0.00
	0.0(3)	7.3	6070(30)	0.555	0.61(2)	0.58	0.57	0.57
	−1.0(3)	6.3	2580(60)	0.639	0.73(2)	0.71	0.70	0.70
	−2.0(3)	5.3	3780(20)	0.773	0.89(3)	0.81	0.81	0.81
	−3.0(1)	4.3	5880(20)	0.852	1.00(3)	0.89	0.88	0.88
Na2	4.7(5)	10.6	4800(90)	0.121	0.07(1)	0.00	0.00	0.00
	0.0(3)	7.3	3430(20)	0.573	0.64(2)	0.56	0.54	0.54
	−1.0(3)	6.3	1640(10)	0.706	0.80(3)	0.70	0.68	0.68
	−2.0(3)	5.3	4980(10)	0.760	0.88(3)	0.80	0.79	0.79
	−3.0(1)	4.3	3325(6)	0.842	0.98(3)	0.88	0.87	0.87
Na3	4.7(5)	10.6	4500(70)	0.131	0.09(1)	0.00	0.00	0.00
	0.0(3)	7.3	3210(30)	0.664	0.75(2)	0.60	0.60	0.60
	−1.0(3)	6.3	4990(20)	0.658	0.75(2)	0.72	0.73	0.73
	−2.0(3)	5.3	4670(20)	0.772	0.89(3)	0.82	0.82	0.83
	−3.0(1)	4.3	3330(70)	0.879	1.0293)	0.89	0.89	0.89
Na4	4.7(5)	10.6	4300(90)	0.121	0.07(1)	0.00	0.00	0.00
	0.0(3)	7.3	2204(6)	0.645	0.73(2)	0.56	0.58	0.57
	−3.0(1)	4.3	2260(20)	0.858	1.00(3)	0.88	0.89	0.88
Na5	4.7(5)	10.6	1750(30)	0.116	0.07(1)	0.00	0.00	0.00
	0.0(3)	7.3	6360(20)	0.559	0.63(2)	0.58	0.54	0.55
	−1.0(3)	6.3	4100(20)	0.673	0.77(2)	0.71	0.68	0.69
	−2.0(3)	5.3	2079(7)	0.771 [a]	0.89(3)	–	–	–
	−3.0(1)	4.3	3330(70)	0.809	0.94(3)	0.89	0.87	0.87
Na6	4.7(5)	10.6	1820(10)	0.146	0.10(1)	0.00	0.00	0.00
	−1.0(3)	6.3	4600(10)	0.663	0.76(2)	0.68	0.67	0.67
	−2.0(3)	5.3	1820(90)	0.747	0.86(3)	0.79	0.78	0.78
	−3.0(1)	4.3	4590(40)	0.840	0.98(3)	0.87	0.86	0.87
MORB	4.7(5)	10.6	2300(100)	0.125	0.08(1)	–	0.08 [b]	–
	0.0(3)	7.3	2230(9)	0.895	1.05(3)	–	0.58 [b]	–
	−1.0(3)	6.3	2220(20)	1.009	1.19(3)	–	0.71 [b]	–
	−2.0(3)	5.3	2179(5)	1.017	1.20(4)	–	0.81 [b]	–
	−3.0(1)	4.3	2170(10)	1.054	1.25(4)	–	0.89 [b]	–
	−7.0(3)	0.3	2250(20)	1.056	1.25(4)	–	0.99 [b]	–
Andesite	4.7(5)	10.6	1375(7)	0.142	0.142 [c]	–	0.09 [b]	–
	0.0(3)	7.3	–	1.194	- [d]	–	0.61 [b]	–
	−1.0(3)	6.3	–	1.160	- [d]	–	0.73 [b]	–
	−2.0(3)	5.3	–	1.171	- [d]	–	0.83 [b]	–
	−3.0(1)	4.3	–	1.185	- [d]	–	0.90 [b]	–
CMAS7G	1200 °C	8.3	–	0.512	0.57(2)	0.46	0.46	0.44
	1300 °C	7.3	–	0.594	0.67(2)	0.58	0.59	0.58
	1400 °C	6.3	–	0.686	0.78(2)	0.67	0.70	0.70
	1500 °C	5.3	–	0.787	0.91(3)	0.75	0.78	0.78

[a] Anomalous intensity, not included in fit.
[b] Predicted using Eq. (11a).
[c] Corrected for beam damage using the change in $I_{1s/4p}$ as a function of time.
[d] Spectra recorded at the APS under conditions where no correction for beam damage was required.

Table 3
The temperature (°C), pressure (GPa), logfO_2 buffer, and calculated logfO_2 (relative to the conventional standard state and fayalite-magnetite-quartz, FMQ) at which hydrous granite, CMAS7G and granite melts were equilibrated for 5 h using a piston cylinder apparatus, the Cu contents (ppm) of the resulting glasses, the raw and beam damage corrected $I_{1s/4p}$ of Cu *K*-edge XANES spectra recorded at the APS, and $Cu^+/\Sigma Cu$ determined from fitting the corrected $I_{1s/4p}$ simultaneously to Eqs. (5), (6), (7) and (8) with melt composition parameterised by NBO/T, optical basicity (Λ) and single cation mole fractions (C_z). Uncertainties of 0.5 and < 0.01 are associated with fO_2 and $Cu^+/\Sigma Cu$.

Sample	Temperature or Pressure	Buffer	logfO_2[a]	ΔFMQ[b]	Cu	$I_{1s/4p}$		$Cu^+/\Sigma Cu$		
						Raw	Cor.	NBO/T	Λ	C_z
Hydrous Granite Temperature Series (1 GPa)										
C5813	900	Pt-PtO_2	> 0.6	>14.1	820(20)	0.104	0.08(1)	0.00	0.00	–
C5813	900	Ru-RuO_2	−4.2	7.8	290(4)	0.468	0.55(2)	0.47	0.51	–
C5805	900	Cu-Cu_2O	−7.2	4.8	2500(200)[c]	1.206	1.27(4)	0.77	0.85	–
C5796	1100	Pt-PtO_2	>2.8	>13.1	2100(30)	0.103	0.08(1)	0.00	0.00	–
C5796	1100	Ru-RuO_2	−2.3	6.7	380(5)	1.000	1.08(3)	0.46	0.63	–
C5795	1400	Pt-PtO_2	4.7	10.6	2240(50)	0.084	0.07(1)	0.00	0.00	–
C5795	1400	Ru-RuO_2	−0.4	5.5	370(3)	0.930	1.00(3)	0.76	0.76	–
CMAS7G Pressure Series (1400 °C)										
C5614	0.5	Pt-PtO_2	4.1	10.2	6900(200)	0.096	0.09(1)	0.37	0.00	0.00
C5761	0.5	Ir-IrO_2	1.7	7.8	4400(50)	0.518	0.53(2)	0.68	0.42	0.41
C5761	0.5	Ru-RuO_2	−0.6	5.6	1192(3)	0.789	0.81(3)	0.00	0.73	0.72
C5612	1.0	Pt-PtO_2	4.7	10.6	7200(100)	0.106	0.10(1)	0.30	0.00	0.00
C5783	1.0	Ir-IrO_2	1.9	7.7	4910(30)	0.461	0.46(2)	0.61	0.37	0.37
C5762	1.0	Ru-RuO_2	−0.4	5.5	1800(20)	0.796	0.81(3)	0.00	0.69	0.68
C5758	2.0	Pt-PtO_2	5.6	10.9	6000(100)	0.096	0.09(1)	0.65	0.00	0.00
C5758	2.0	Ir-IrO_2	2.2	7.5	4750(20)	0.425	0.42(2)	0.87	0.32	0.32
C5758	2.0	Ru-RuO_2	−0.1	53	1988(8)	0.696	0.70(2)	0.00	0.63	0.64
C5759	2.5	Pt-PtO_2	6.0	11.0	5870(80)	0.106	0.09(1)	0.71	0.00	0.00
C5759	2.5	Ir-IrO_2	2.4	7.4	4800(100)	0.421	0.43(2)	0.90	0.32	0.32
C5759	2.5	Ru-RuO_2	0.1	5.1	2710(60)	0.737	0.75(2)	0.00	0.63	0.64
Granite Pressure Series (1400 °C)										
C5788	0.5	Pt-PtO_2	4.1	10.2	2040(60)	0.155	0.14(1)	0.73	0.00	–
C5790	0.5	Ir-IrO_2	1.7	7.8	630(10)	0.781	0.81(3)	0.91	0.65	–
C5790	0.5	Ru-RuO_2	−0.6	5.6	400(15)	1.081	1.11(3)	0.00	0.87	–
C5769	1.0	Pt-PtO_2	4.7	10.6	1270(20)	0.135	0.12(1)	0.68	0.00	–
C5769	1.0	Ir-IrO_2	1.9	7.7	320(20)	0.944	0.97(3)	0.89	0.69	–
C5769	1.0	Ru-RuO_2	−0.4	5.5	210(7)	1.022	1.08(3)	0.98	0.89	–
C5770	2.0	Pt-PtO_2	5.6	10.9	1290(70)	0.175	0.17(1)	0.00	0.00	–
C5770	2.0	Ir-IrO_2	2.2	7.5	280(30)	0.980	1.00(3)	0.61	0.71	–
C5770	2.0	Ru-RuO_2	−0.1	53	260(10)	1.000	1.00(3)	0.90	0.90	–
C5791	2.5	Pt-PtO_2	6.0	11.0	2700(60)	0.127	0.12(1)	0.00	0.00	–
C5791	2.5	Ir-IrO_2	2.4	7.4	920(40)	0.859	0.86(3)	0.67	0.67	–
C5791	2.5	Ru-RuO_2	0.1	5.1	770(40)	1.129	1.16(3)	0.00	0.88	–
C5757	2.5	Re-ReO_2	−3.5	1.5	10500(100)[c]	1.185	1.20(4)	0.74	0.98	–

[a] The fO_2 imposed by Pt-PtO_2 was calculated using the equation of state of O_2 (Belonoshko and Saxena, 1991), which applies at P-T where PtO_2 decomposes to Pt and O_2. At other conditions this fO_2 represents the minimum value. The chemical potential of O_2 at each temperature and the molar volumes of the metal and metal oxide were used to calculate the fO_2 imposed by Ir-IrO_2, Ru-RuO_2 (O'Neill and Nell, 1997), Re-ReO_2 (Pownceby and O'Neill, 1994) and Cu-Cu_2O (O'Neill and Pownceby, 1993; Holland and Powell, 2001). See Appendix G in Miller 2020 for more details.

[b] ΔFMQ = logfO_2 – (8.58–25050/T + 940*P/T-0.02*P), where P is in GPa and T in K (Ballhaus et al., 1991; O'Neill et al., 2018).

[c] A $Cu_{15}Pd_{85}$ capsule was used in these experiments. The high Cu contents reflect the solubility of Cu under the experimental conditions.

The Cu *K*-edge XANES spectra, recorded at the AS, of CMAS7G samples prepared over a temperature range of 1200 to 1500 °C at logfO_2 = 0 are shown in Fig. 1c. The spectra recorded at the APS of hydrous granite samples prepared over a temperature range of 900 to 1400 °C at various fO_2s are shown in Fig. S5. The intensity of the $1s \rightarrow 4p$ peak ($I_{1s/4p}$) increases with increasing temperature indicating that Cu^+ is stabilised relative to Cu^{2+} at higher temperatures (Fig. 1c).

All of the spectra for the pressure series samples were recorded at the APS. The spectra of CMAS7G samples equilibrated at 2.5 GPa are shown in Fig. 1d. The spectra of the CMAS7G and granite pressure series samples are shown in Fig. S6 and S7, respectively. The fO_2s imposed by the metal–metal oxide buffers change with pressure, and the effect of pressure on $Cu^+/\Sigma Cu$ needs to be deconvolved from this. The spectra recorded from samples equilibrated with Pt-PtO_2 do not exhibit a peak at 8984 eV and record the presence of solely Cu^{2+} (black spectra; Figs. 1d; S5). The spectra recorded from samples equilibrated with Ir-IrO_2 and Ru-RuO_2 exhibit a peak at ~8984 eV. The peak is more intense in the samples equilibrated with Ru-RuO_2 indicating higher $Cu^+/\Sigma Cu$, than those equilibrated with Ir-IrO_2 (red and blue spectra; Figs. 1d, S5), which is qualitatively consistent with the difference in fO_2 imposed by these buffers.

XANES spectra of the Fe-bearing redox series compositions (MORB and andesite) are shown in Fig. 2. The spectra for the MORB and andesite glasses were recorded at the AS and APS, respectively. The spectra exhibit the same features as those observed for the CNMAS redox series glasses. However, in contrast, $I_{1s/4p}$ and the shape of the main edge remain relatively constant for all samples equilibrated at ΔFMQ ≤ 0 (Fig. 2).

4.2. Beam damage

The $1s \rightarrow 4p$ peak exhibits a large range in intensity with fO_2, meaning that it is particularly sensitive to changes in the oxidation state of Cu (Fig. 1), and was selected as the feature to assess beam damage. At the APS $I_{1s/4p}$ was monitored as a function of time. At zero time $I_{1s/4p}$ reflects the true oxidation state of the sample, while after exposure to the beam changes in $I_{1s/4p}$ reflect the amount and direction (oxidation/reduction) of beam damage. Examples of changes in intensity due to beam damage are shown in Fig. S8. Using a focused beam samples equilibrated at atmospheric pressure exhibited beam damage, which was mitigated by defocusing and attenuating the beam by placing Al foil in the beam path. Samples equilibrated at pressures greater than

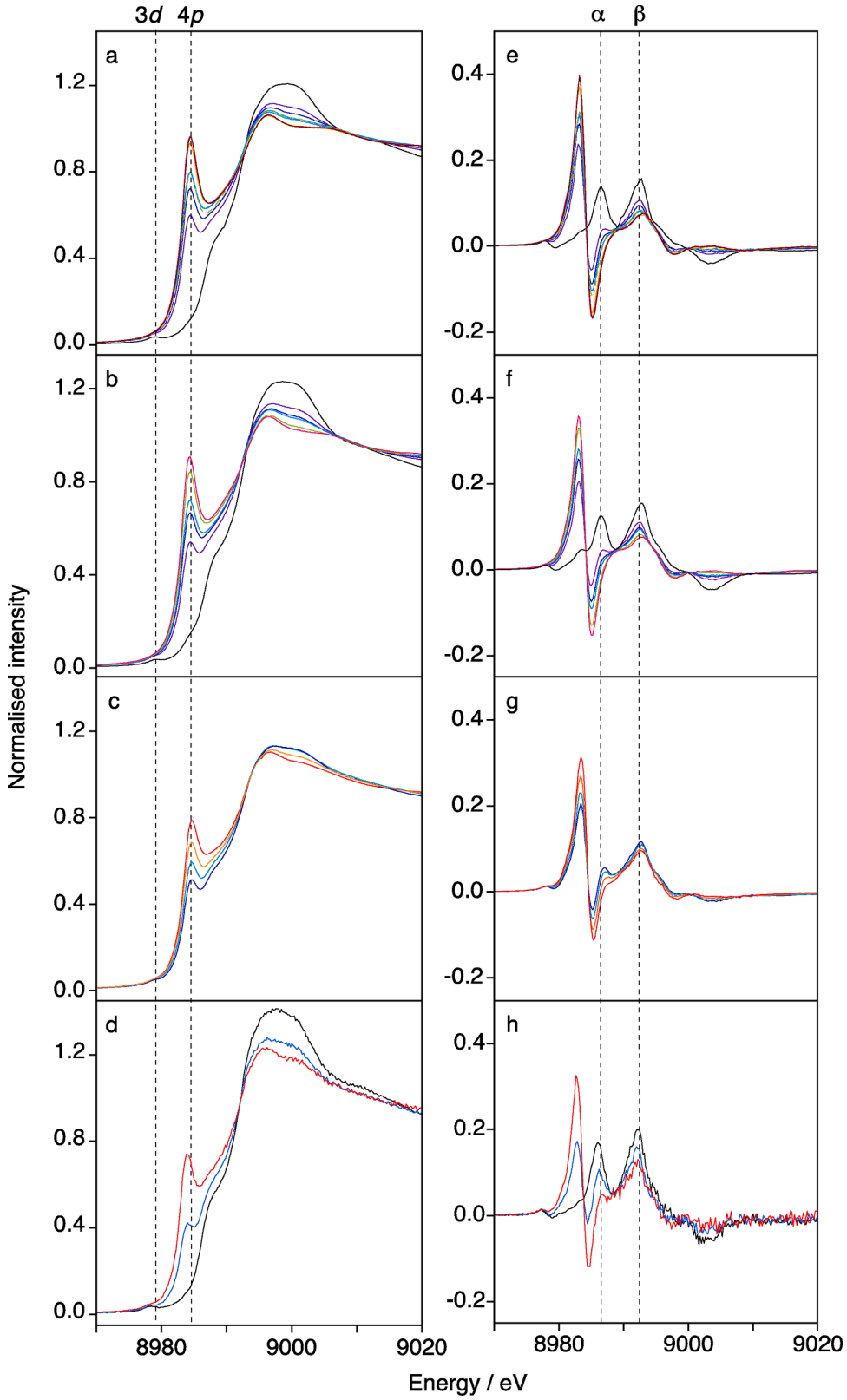

Fig. 1. (a-d) Cu *K*-edge XANES spectra and (e-h) the corresponding derivative spectra recorded from **(a, e)** CMAS7G, and **(b, f)** Osborn5 compositions equilibrated at 1400 °C, 1.0 GPa and ΔFMQ = 11 (black) and 1300 °C, atmospheric pressure and ΔFMQ = 7.3 (purple), 6.3 (dark blue), 5.3 (light blue), 4.3 (green), 2.3 (yellow), 1.3 (orange), 0.3 (pink) and −0.7 (red), **(c, g)** CMAS7G equilibrated at atmospheric pressure, logfO_2 = 0 and 1200 °C (ΔFMQ = 8.3; dark blue), 1300 °C (ΔFMQ = 7.3; light blue), 1400 °C (ΔFMQ = 6.3; orange) and 1500 °C (ΔFMQ = 5.3; red), and **(d, h)** CMAS7G equilibrated at 1400 °C, 2.5 GPa and ΔFMQ = 11.0 (Pt-PtO_2: black), 7.4 (Ir-IrO_2: blue) and 5.1 (Ru-RuO_2: red). Dashed lines in (a-d) indicate the energy of the 1*s*-3*d* and 1*s*-4*p* transitions and in (e-h) the α and β peaks. The reader is referred to the online article for the colour version of this figure.

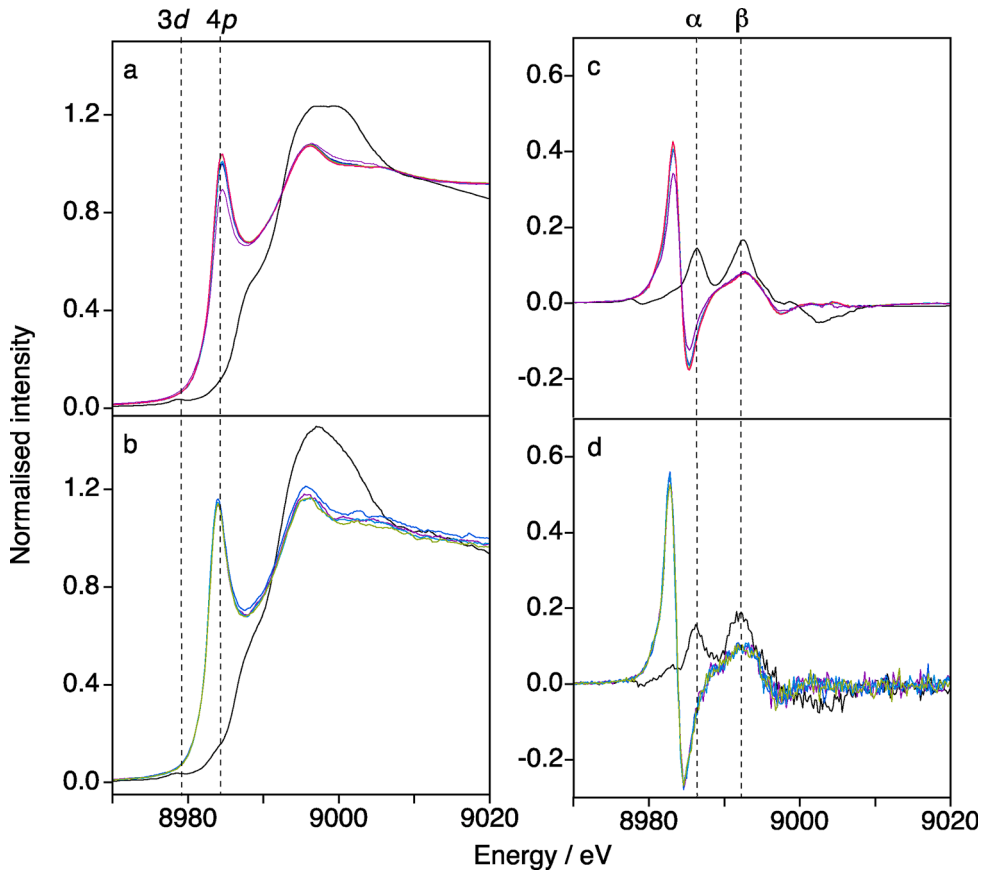

Fig. 2. (a, b) Cu *K*-edge XANES spectra and (c, d) the corresponding derivative spectra recorded from **(a, c)** MORB and **(b, d)** andesite equilibrated at 1400 °C, 1.0 GPa, and ΔFMQ = 11 (black) and 1300 °C, atmospheric pressure and ΔFMQ = 7.3 (purple), 6.3 (dark blue), 5.3 (light blue), 4.3 (green) and 0.3 (pink). Dashed lines in (a, b) indicate the energy of the 1*s*-3*d* and 1*s*-4*p* transitions and in (c, d) the α and β peaks. The reader is referred to the online article for the colour version of this figure.

atmospheric exhibited beam damage despite these measures. It was not possible to prevent this beam damage as further attenuation of the beam resulted in spectra with poor signal-to-noise. The $I_{1s/4p}$ recorded as a function of time from these glasses increased for oxidised samples (Pt-PtO_2 buffer; Fig. S8a,c) and decreased for reduced samples (≤Ir-IrO_2 buffer; Fig. S8b,d). As $I_{1s/4p}$ scales with the proportion of Cu^+ this indicates that exposure to the beam caused reduction of highly oxidised and oxidation of all other samples.

The wake-up time of the 100 element Ge detector at the AS (i.e., the time taken for a detector to reach a steady value after exposure to X-rays) was slower than the timescale of beam damage such that it was not possible to use changes in intensity at a fixed energy to check for beam damage. The spectra recorded from samples equilibrated at atmospheric pressure at the APS were not affected by beam damage and a comparison of the spectra recorded at the two beamlines was used to identify beam damage at the AS. The spectra recorded at the APS of samples equilibrated at $\log fO_2 \leq 0$ (FMQ ≤ 7.3) have a higher intensity at both the energy of the $1s \rightarrow 4p$ feature (indicating more Cu^+) and the main edge (indicating more Cu^{2+}; Fig. S9). As it is not possible for beam damage to cause an increase in both Cu^+ and Cu^{2+} these differences in intensity are attributed to differences in beamline resolution and/or detector dead-time correction. For samples equilibrated at FMQ ≤ 5.3 the differences in $1s \rightarrow 4p$ intensity are larger than can be explained by purely differences in beamline instrumentation (Fig. S9) and are attributed to beam damage at the AS.

4.3. *Evaluating $Cu^+/\Sigma Cu$ from the spectra*

The oxidation state of a redox variable element can be quantified through the identification and parametrisation of a redox variable spectral feature (e.g., Berry et al., 2004; Burnham et al., 2015; Berry et al., 2018) or by linear combination fitting of end-member spectra (LCF; e.g., Miller et al., 2019; Berry et al., 2021). Here we chose the former method, using the intensity of the $1s \rightarrow 4p$ peak, firstly because the scans of $I_{1s/4p}$ with time recorded at the APS enable a beam damage correction, and secondly because a single spectral feature enables an easy comparison of the spectra recorded at the APS and AS. The success of this method has been demonstrated by previous studies (e.g., Berry et al., 2004; Burnham et al., 2015; Berry et al., 2018).

The percentage change in $I_{1s/4p}$ over the time taken to reach the energy of the $1s \rightarrow 4p$ peak was determined for each intensity time scan. The measured $I_{1s/4p}$ of the spectra recorded at the APS were then corrected by this amount to "remove" the effects of beam damage. The uncorrected and corrected $I_{1s/4p}$ are given in Table 3.

The $I_{1s/4p}$ of spectra recorded at the APS are compared to those recorded at the AS for 38 samples in Fig. S10. The $I_{1s/4p}$ define a linear trend that is offset from a 1:1 line. This offset is considered to be mainly due to beam damage. The scatter around a linear trend increases with intensity (Fig. S10) and the uncertainties (s) in $I_{1s/4p}$ are assumed to have the form:

$$s\left(I_{1s/4p}\right) = s_0 + s_1\left(I_{1s/4p}\right) \quad (1)$$

where s_0 is a constant associated with determining the baseline of $I_{1s/4p}$ and s_1 scales with the value of $I_{1s/4p}$. A value of 0.005 was estimated for

s_0 based on the variability of the intensity at 8984 eV for samples with $Cu^+/\Sigma Cu \approx 0$. Part of this variation will be due to the effect of composition (Kau et al., 1987). Fitting a line to the data, with s_0 fixed as 0.005 and assuming a reduced chi-squared (χ^2_υ) of 1, gives $s_1 = 0.02$ if the uncertainties in $I_{1s/4p}$ from the AS and APS spectra are assumed to be the same. The beam damage affecting the AS spectra argues against such equal uncertainties and instead values of s_1 of 0.015 and 0.025 were assigned respectively to the APS and AS $I_{1s/4p}$. Using the resulting uncertainties in each $I_{1s/4p}$ (Eq. (1) the correlation between $I_{1s/4p}$ at the APS and AS (shown in Fig. S10) is given by:

$$I_{1s/4p}(\mathrm{APS}) = I_{1s/4p}(\mathrm{AS})*1.26 - 0.08 \quad (2)$$

Eq. (2) enables the $I_{1s/4p}$ of spectra recorded at the AS to be corrected for beam damage (and differences in spectral resolution), resulting in $I_{1s/4p}$ that are consistent with those recorded at the APS. The uncorrected and corrected $I_{1s/4p}$ for each spectrum are given in Table 2.

The oxidation of Cu^+ to Cu^{2+} is given by the reaction $\frac{1}{2}Cu_2O + \frac{1}{4}O_2 \rightarrow CuO$ and hence $Cu^+/\Sigma Cu$ should vary with fO_2 according to the sigmoidal relationship:

$$Cu^+/\Sigma Cu = \frac{1}{1 + 10^{(0.25\log fO_2 + \log K')}} \quad (3)$$

where K' is a modified equilibrium constant (see Berry and O'Neill 2004). Spectral features that correspond to a single oxidation state, such as the $1s \rightarrow 4p$ peak, should be linearly related to $Cu^+/\Sigma Cu$:

$$Cu^+/\Sigma Cu = a_0 + a_1\left(I_{1s/4p}\right) \quad (4)$$

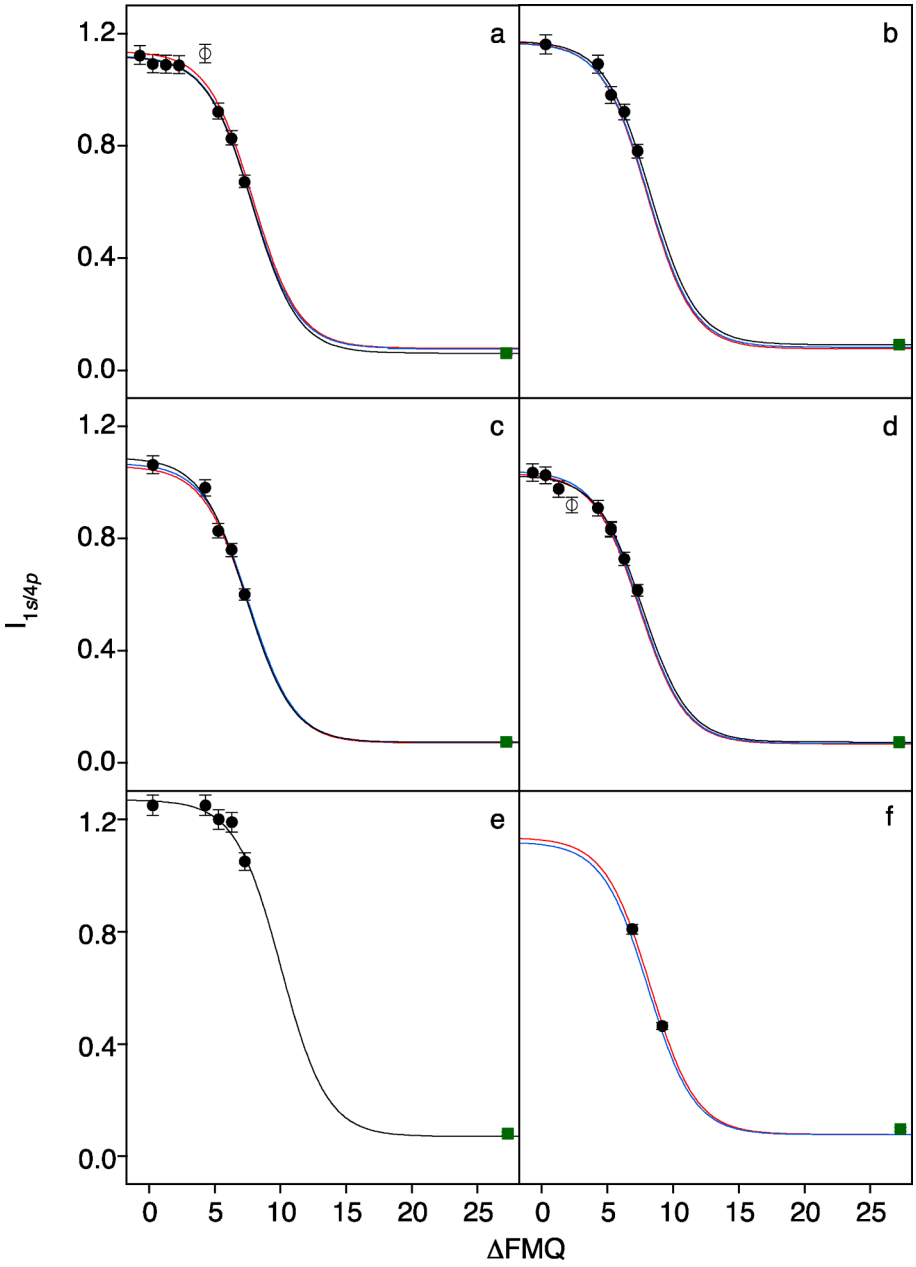

Fig. 3. The corrected $I_{1s/4p}$ (solid circles) and anomalous $I_{1s/4p}$ (open circles) of XANES spectra recorded from **(a)** CMAS7G, **(b)** Longhi4, **(c)** Osborn5 **(d)** CAS1 and **(e)** MORB equilibrated at 1300 °C and atmospheric pressure, and **(f)** CMAS7G equilibrated at 1400 °C and 1 GPa. The fits of Eq. (5) (black; a, b, c, d, e), and simultaneous fits of Eqs. (5), (6), (7) and (8) with melt composition parametrised by optical basicity (red) and single cation mole fractions (blue) are shown. The baseline of $I_{1s/4p}$ (green squares) is constrained by samples containing $Cu^+/\Sigma Cu = 0$ and this $I_{1s/4p}$ was included in the fits at $\Delta FMQ = 27$ so that only the intensity and not the position of the sigmoid relative to $\log fO_2$ was constrained. The reader is referred to the online article for the colour version of this figure.

where a_0 and a_1 are constants that depend on the coordination environments of Cu^+ and Cu^{2+} (and hence composition and pressure). The minimum intensity at the energy of $I_{1s/4p}$, which occurs when $Cu^+/\Sigma Cu = 0$, is dependent on the coordination environment of Cu^{2+}, and the maximum value, which occurs when $Cu^+/\Sigma Cu = 1$, is dependent on the coordination environment of Cu^+. The minimum value of $I_{1s/4p}$ is thus $-a_0/a_1$ and the maximum $(1-a_0)/a_1$. Substituting Eq. (4) into Eq. (3) gives:

$$I_{1s/4p} = (1/(1 + 10^{(0.25\log fO_2 + \log K')}) - a_0) / a_1 \quad (5)$$

The $I_{1s/4p}$ (Table 2, S1) for the redox series samples equilibrated at 1 atmosphere were fitted to Eq. (5). However, by plotting peak intensity as a function of fO_2 it is apparent that there are no data at the fO_2s where $Cu^+/\Sigma Cu \approx 0$, and hence the fits were not well constrained (Fig. 3). Thus, it was necessary to constrain the vertical range of the sigmoid by including a baseline intensity where $Cu^+/\Sigma Cu = 0$. The spectra recorded from glasses equilibrated at 1400 °C, 1 GPa and ΔFMQ = 11 show no evidence of Cu^+ (black spectra in Fig. 1) and were used to define the background intensity. Potentially, Cu^{2+} may have a different coordination environment in the samples equilibrated at 1 GPa to those equilibrated at atmospheric pressure, however, the spectra recorded from these samples pass through the isosbestic points defined by the samples equilibrated at atmospheric pressure suggesting that any difference is insignificant (Fig. 1, S3, S4). Further, linear combination fits using 1 GPa spectra as the oxidised end-member were able to reproduce the spectra of samples equilibrated at atmospheric pressure (Fig. S11).

The corrected $I_{1s/4p}$ for the redox series glasses, including the background $I_{1s/4p}$ at $\log fO_2 = 4.7$ (ΔFMQ = 11), were fitted to Eq. (5). These fits indicated that the $\log fO_2 = 4.7$ samples contain less Cu^+ than would be expected at that fO_2. This suggests that something other than the fO_2 of equilibration has affected the oxidation state of Cu in these samples. Electron exchange reactions between redox variable elements, in particular with Fe, can occur on cooling (e.g., Berry et al., 2003b; Burnham and Berry, 2014; Miller et al., 2019; Berry et al., 2021) as at high temperatures entropy promotes a mixture of oxidation states, which on cooling are not stable. In this case, while no other redox variable element was intentionally included in the system the samples equilibrated under the most oxidised conditions contain significant Pt (3000 to 6000 ppm). The Ir, Ru and Re contents of the glasses are insufficient to have an effect. The Pt contents of the glasses suggest that the majority of Pt is dissolved as Pt^{2+} (Fortenfant et al., 2003). The redox potentials of $Pt^{4+/2+}/Pt^0$ and Cu^{2+}/Cu^+ determined for a silicate melt at 1400 °C (Schreiber et al., 1999) suggest that the electron exchange reaction $2Cu^+ + Pt^{2+} \rightarrow 2Cu^{2+} + Pt^0$ could have occurred. The number of moles of Pt^{2+} present in the samples equilibrated at ΔFMQ = 11 is more than the predicted number of moles of Cu^+ and hence sufficient to completely react with and remove Cu^+ from the melt. The solubility of Pt decreases with decreasing fO_2 such that the samples equilibrated in Pt capsules at lower fO_2s do not contain enough Pt for an electron exchange reaction to significantly affect Cu^+/Cu^{2+}. Although the spectra recorded from the samples equilibrated at ΔFMQ = 11 give quench-modified Cu^+/Cu^{2+}, the resulting Cu^{2+} only spectra can be used to constrain the minimum intensity of $I_{1s/4p}$. The $I_{1s/4p}$ of the Pt-PtO_2 samples were included in the fits at $\log fO_2 = 20$, since at this fO_2 Eq. (3) would require all Cu to be present as Cu^{2+} ($Cu^+/\Sigma Cu$ would change from 0.05 to 0.95 over 9.6 log units). Representative fits are shown in Fig. 3.

Rather than fitting each redox series individually a global fit that simultaneously parameterises the effects of fO_2, composition, temperature and pressure on $Cu^+/\Sigma Cu$ represents a more robust approach as the effects of anomalous data are minimised. The Fe-bearing samples should not be included in this fit due to the possibility of a Fe-Cu electron exchange (e.g., Miller et al., 2019). The corrected $I_{1s/4p}$ for the MORB and andesite compositions were thus fit to Eq. (5) individually. The maximum $I_{1s/4p}$ and $\log K'$ determined for MORB are 1.28(4) and −0.69 (9), respectively (Table 5), and the fit is shown in Fig. 3e. The fit of the corrected $I_{1s/4p}$ of the andesite series to Eq. (5) was poor as the $I_{1s/4p}$ do not vary with fO_2 in the expected manner, being constant for samples equilibrated at $\log fO_2 = 0, -1, -2$ and -3 (Fig. 2b). A maximum $I_{1s/4p}$ of 1.161(1) was determined from the spectra.

Table 4
The parameters determined by fitting the corrected $I_{1s/4p}$ simultaneously to Eqs. (5), (6), (7) and (8) with melt composition parameterised by NBO/T, optical basicity (Λ) and single cation mole fractions (c_z). The standard error of the parameters and χ^2_ν of the fits are given.

Parameter	NBO/T	Λ	c_z
b_0	−0.07(1)	−0.01(7)	−0.07(1)
b_1	0.003(16)	0.10(11)	0.02(5)
d_0	0.86(3)	−0.02(17)	0.80(4)
d_1	0.15(4)	1.65(29)	0.64(27)
C	0.21(8)	1.99(55)	–
e	−3.30(39)	−4.73(50)	−3.74(45)
f	5000(600)	5400(500)	5300(700)
SiO_2	–	0.48[a]	–
Al_2O_3	–	0.60[a]	−0.21(20)
MgO	–	0.78[a]	0.68(20)
CaO	–	1.00[a]	1.07(20)
Na_2O	–	1.15[a]	0.90(26)
K_2O	–	1.40[a]	–
H_2O	–	0.40[a]	–
v_0 (CMAS)	−250(240)	280(190)	270(260)
v_1 (CMAS)	120(120)	−90(90)	−90(100)
v_0 (Granite)	−940(450)	−760(400)	–
v_1 (Granite)	250(200)	190(160)	–
χ^2_ν	1.95	1.35	1.28

[a] Not determined in the fit; Λ_z values from Lebouteiller and Courtine (1998) and Moretti and Ottonello (2003).

The coordination environments of Cu^+ and Cu^{2+} will vary as a function of composition and pressure such that terms for the effect of these variables on a_0 and a_1 need to be included in a global fit. The coordination environments will be those at the glass transition temperature, which at a given pressure will be constant for each composition and independent of the temperature of melt equilibration (assuming similar cooling rates through the glass transition), meaning that a term for the effect of temperature is not necessary. Following Berry et al. (2021) the compositional dependence of the coordination environments of Cu^{2+} and Cu^+ can be parameterised by:

$$a_0 = b_0 + b_1 C \quad (6)$$

$$a_1 = d_0 + d_1 C \quad (7)$$

where b_0, b_1, d_0 and d_1 are compositional parameters of the glasses, and C a chemical or structural parameterisation of melt composition (e.g., NBO/T, Λ).

The spectra recorded from CMAS7G and granite compositions equilibrated under the most oxidised conditions of our experiments (ΔFMQ > 10) and at all pressures (> 0.5 GPa) investigated only indicate the presence of Cu^{2+}. The standard deviation of $I_{1s/4p}$ for these spectra is 0.018 (1.5% of the maximum intensity). This indicates that any changes in the coordination environment of Cu^{2+} with pressure do not significantly affect the minimum value of $I_{1s/4p}$. Further, linear combination fitting using a Cu^+ end-member spectrum recorded from a CMAS7G sample equilibrated at atmospheric pressure, and a Cu^{2+} end-member spectrum recorded from CMAS7G equilibrated under oxidising condition at a particular pressure, were able to reproduce the spectra of samples equilibrated at that pressure with mixed Cu oxidation states (Fig. S11). This indicates that the coordination environment of Cu^+, and the maximum intensity of $I_{1s/4p}$, does not change significantly over this pressure range (0 to 2.5 GPa), and hence no term to account for the effect of pressure on the coordination environments of either Cu^+ or Cu^{2+} was included.

The modified equilibrium constant, K', varies as a function of

Table 5
$\log K'$ for the reaction $Cu_2O + 1/2O_2 = 2CuO$ at 1300 °C and atmospheric pressure, and the maximum intensity of $I_{1s/4p}$, determined from fitting the corrected $I_{1s/4p}$ simultaneously to Eqs. (5), (6), (7) and (8) with melt composition parameterised by NBO/T, optical basicity (Λ) and single cation mole fractions (c_z), the energy (eV) of the $1s \rightarrow 4p$ peak of Cu^+, and the energy and intensity of the α and β peaks of Cu^{2+} (and the energy difference, α-β), determined from the most reduced and oxidised spectra, respectively, for each composition. An uncertainty of 0.01 is associated with the energy values and 0.001 with the intensities of α and β.

Composition	$\log K'$			$1s \rightarrow 4p$			α		β		α-β
	NBO/T	Λ	c_z	Energy	Max int.Λ	Max int. c_z	Energy	Intensity	Energy	Intensity	
AnDi	−0.07	−0.10	−0.10	8984.45	1.09	1.08	8986.51	0.143	8992.55	0.158	6.04
CMAS7G	−0.13	−0.16	−0.14	8984.39	1.14	1.12	8986.26	0.143	8992.50	0.158	6.24
Longhi2	−0.06	−0.08	−0.06	8984.59	1.07	1.06	8986.26	0.135	8992.40	0.157	6.13
Longhi3	−0.18	−0.21	−0.25	8984.72	1.19	1.21	8986.67	0.148	8992.61	0.161	5.94
Longhi4	−0.17	−0.19	−0.20	8984.43	1.17	1.17	8986.87	0.137	8992.93	0.155	6.06
Osborn1	−0.06	−0.07	−0.07	8984.30	1.06	1.06	8986.48	0.124	8992.68	0.153	6.20
Osborn3	−0.05	−0.10	−0.09	8984.39	1.09	1.08	8986.50	0.125	8992.70	0.153	6.20
Osborn4	−0.05	−0.08	−0.07	8984.35	1.07	1.06	8986.59	0.128	8992.77	0.155	6.18
Osborn5	−0.07	−0.07	−0.08	8984.31	1.06	1.07	8986.53	0.128	8992.79	0.155	6.26
Osborn6	−0.11	−0.14	−0.16	8984.52	1.12	1.14	8986.43	0.133	8992.54	0.158	6.10
CAS1	−0.08	−0.04	−0.04	8984.49	1.03	1.04	8986.16	0.133	8992.55	0.155	6.39
CAS4	−0.10	−0.10	−0.08	8984.49	1.09	1.07	8986.36	0.134	8992.34	0.158	5.97
CAS5	−0.18	−0.18	−0.19	8984.39	1.16	1.16	8986.66	0.130	8992.72	0.153	6.06
Na1	−0.14	−0.12	−0.12	8984.35	1.10	1.10	8986.61	0.136	8992.63	0.157	6.01
Na2	−0.11	−0.06	−0.08	8984.45	1.06	1.07	8986.27	0.124	8992.54	0.154	6.26
Na3	−0.14	−0.07	−0.09	8984.42	1.15	1.15	8986.60	0.140	8992.85	0.158	6.24
Na4	−0.17	−0.17	−0.18	8984.42	1.12	1.10	8986.61	0.129	8992.48	0.153	5.87
Na5	−0.11	−0.14	−0.12	8984.39	1.06	1.08	8986.30	0.131	8992.42	0.159	6.12
Na6	−0.08	−0.05	−0.06	8984.38	1.04	1.05	8986.24	0.122	8992.55	0.156	6.30
Granite	–	–	–	8984.48	1.27	1.18	8986.15	0.188[a]	8992.00	0.218[a]	5.29
Hydrous granite	–	–	–	8984.48	1.30	1.37	8987.09	0.175[a]	8992.94	0.209[a]	4.95
MORB	–	−0.690[b]	−0.14[d]	8984.61	1.28[b]	–	8986.50	0.144	8992.61	0.167	6.11
Andesite	–	-[c]	−0.19[d]	8984.71	1.16[e]	–	8987.16	0.123	8993.04	0.159	5.88

[a] Determined from spectra recorded at the APS.
[b] Determined from fitting the corrected $I_{1s/4p}$ to Eq. (5).
[c] Could not be determined.
[d] Predicted using Eq. (11a).
[e] Determined directly from the spectra.

composition, temperature (T) and pressure (P), and following O'Neill and Berry (2021) has the form:

$$\log K' = e + f/T + C + \left(v_0 P + v_1 P^2\right)/T \quad (8)$$

where e is a constant (an entropy-like term), f (an enthalpy-like term) describes the dependence on temperature (K), C parameterises the effect of composition, and v_0 and v_1 describe the dependence on pressure (GPa).

The corrected $I_{1s/4p}$ of the spectra for the Fe-free redox, temperature and pressure series glasses (Tables 2, 3) were fit to Eq. (5) with a_0, a_1 and $\log K'$ defined by Eqs. (6), (7), and (8), respectively, using least squares minimisation. The fit was performed with C defined in three ways: (i) C = c*NBO/T, (ii) C = c*Λ and (iii) $C = \Sigma c_z X_z$, where c is a scaling factor, c_z is a constant for each cation (z) and X_z the mole fraction of each cation defined on a single-cation basis (e.g., MgO, $AlO_{3/2}$, $NaO_{1/2}$). NBO/T and Λ can be calculated from the compositions (Table 1) and their evaluation, and that of the single-cation mole fractions, are given in Supplementary Information 1. The c_z are unknowns, and as there are only two K_2O-bearing melts and one H_2O-bearing melt, it was not possible to refine the compositional effect of K_2O or H_2O. As a result, the single-cation mole fraction model was only fit to the CNMAS redox, and CMAS7G temperature and pressure series data. A c_z term for SiO_2 was not included in the single-cation mole fraction model as the mole fractions are defined to sum to one. Initial fitting of the models using NBO/T and Λ revealed that the effect of pressure on $Cu^+/\Sigma Cu$ was different for the CMAS7G and granite compositions. As the effect of pressure was only investigated for two compositions the v_0 and v_1 parameters were determined separately for each composition.

Eleven $I_{1s/4p}$ were identified as anomalous as the spectra of these samples did not pass through the isosbestic points defined by their compositional series (these are indicated in Table 2) and were not included in the fit. This resulted in 150 observations, with 11 parameters to be refined when the composition was parameterised by NBO/T or Λ, and 138 degrees of freedom. The single-cation mole fraction model had 130 observations, 12 parameters to be refined and 125 degrees of freedom. The $I_{1s/4p}$ were weighted according to the uncertainties in fO_2 (Tables 2, 3) and Eq. (1). The fits were carried out in Python and the associated code and input data is provided as supplementary material. The refined parameters and χ^2_ν are given in Table 4.

Table 6
$\log K'$ for the reaction $Cu_2O + 1/2O_2 = 2CuO$ for a range of temperatures and pressures determined from fitting the corrected $I_{1s/4p}$ simultaneously to Eqs. (5), (6), (7) and (8) with melt composition parameterised by NBO/T, optical basicity (Λ) and single cation mole fractions (c_z). The hydrous granite and granite series were not fit to the c_z model.

Temperature/°C	Pressure/GPa	$\log K'$		
		NBO/T	Λ	c_z
CMAS7G Temperature Series				
1200	Atmospheric	0.07	0.08	0.08
1300	Atmospheric	−0.13	−0.16	−0.14
1400	Atmospheric	−0.32	−0.36	−0.34
1500	Atmospheric	−0.48	−0.54	−0.52
Hydrous Granite Temperature Series				
900	1.0	0.85	1.03	–
1100	1.0	0.27	0.33	–
1400	1.0	−0.35	−0.39	–
CMAS7G Pressure Series				
1400	0.5	−0.37	−0.29	−0.28
1400	1.0	−0.39	−0.24	−0.23
1400	2.0	−0.32	−0.23	−0.23
1400	2.5	−0.23	−0.26	−0.27
Granite Pressure Series				
1400	0.5	−0.69	−0.69	–
1400	1.0	−0.86	−0.83	–
1400	2.0	−0.98	−0.94	–
1400	2.5	−0.92	−0.90	–

The χ^2_ν of the models using NBO/T, Λ and single-cation mole fractions models are 1.95, 1.35 and 1.28, respectively. Accordingly, the calculated versus observed $I_{1s/4p}$ show the greatest misfit for the NBO/T model (Fig. S12). The larger χ^2_ν of the NBO/T model indicates that this way of parameterising melt composition is less effective at describing how composition effects the oxidation state of Cu. $Cu^+/\Sigma Cu$ determined by these models are given in Tables 2 and 3 and the logK' in Tables 5 and 6. The maximum $I_{1s/4p}$ predicted by each model are given in Table 5. Representative fits are shown in Fig. 3.

That the χ^2_ν of the Λ model is larger than that of the single-cation mole fraction model is unsurprising given that Λ is fixed for each composition whereas the c_z are variables within the fitting process. The c_z exhibit a positive correlation (R = 0.86; where R is the correlation coefficient) with the Λ_z of the oxides (given in Table 4; Fig. S13a). The slope of the correlation is 2.0(8), which corresponds to the value of the scaling factor, c, determined for the optical basicity model (1.99(54); Table 4). $Cu^+/\Sigma Cu$ and logK' determined by the two models have, within error, 1:1 correlations with correlation coefficients of 0.99 (Fig. S13b,c). This, in addition to the linear correlation between the c_z and Λ_z, and the similar χ^2_ν, indicates that the results of the two models are essentially identical and that the effect of composition on $Cu^+/\Sigma Cu$ can be effectively modelled using either Λ or single-cation mole fractions.

Substituting Eq. (8) into Eq. (3) and rewriting Eq. (3) as $\log(Cu^{2+}/Cu^+) = 0.25\log fO_2 + \log K'$ allows a general expression for the oxidation state of Cu to be derived for the Λ compositional model:

$$\log\left(Cu^{2+}/Cu^{+}\right) = 0.25\log fO_2 - 4.73 + 5400/T + 1.99\Lambda + \left(280P - 90P^2\right)/T \quad (9a)$$

and using single-cation mole fractions:

$$\log\left(Cu^{2+}/Cu^{+}\right) = 0.25\log fO_2 - 3.74 + 5300/T + \left(-0.21X_{Al_2O_3} + 0.68X_{MgO} + 1.07X_{CaO} + 0.90X_{Na_2O}\right) + (270P - 90P^2)/T \quad (9b)$$

The fO_2 of FMQ is given by (Ballhaus et al., 1991; O'Neill et al., 2018):

$$\log fO_2(FMQ) = 8.58 - 25050/T \quad (10a)$$

or

$$\log fO_2(FMQ) = 8.58 - 25050/T + 940P/T - 0.02P \quad (10b)$$

The fO_2 in Eqs. (9a) and (9b) (relative to O_2 at 1 bar and the temperature of interest) can be converted to values relative to FMQ (ΔFMQ) at either 1 bar and the temperature of interest, or the temperature and pressure of interest, by subtracting Eq. (10a) or (10b), respectively. This gives:

$$\log\left(Cu^{2+}/Cu^{+}\right) = 0.25(\Delta FMQ + 8.58 - 25050/T + 940P/T - 0.02P) - 4.73 + 5400/T + 1.99\Lambda + \left(280P - 90P^2\right)/T \quad (11a)$$

and

$$\log(Cu^{2+}/Cu^{+}) = 0.25(\Delta FMQ + 8.58 - 25050/T + 940P/T - 0.02P) - 3.74 + 5300/T + (-0.21X_{Al_2O_3} + 0.68X_{MgO} + 1.07X_{CaO} + 0.90X_{Na_2O}) + (270P - 90P2)/T \quad (11b)$$

Eqs. (11a) and (11b) allow the oxidation state of Cu to be predicted for a range of silicate melt compositions, temperatures (900–1500 °C) and pressures (0 to 2.5 GPa). The c_z have only been determined for the oxide components of the melts studied, whereas Λ can be calculated for compositions containing other oxides that are commonly present in silicate melts (Lebouteiller and Courtine, 1998).

5. Discussion

5.1. The effect of composition, temperature and pressure on $Cu^+/\Sigma Cu$

The effect of melt composition on $Cu^+/\Sigma Cu$ was investigated by using the parameterisations NBO/T, Λ and single-cation mole fractions. NBO/T is calculated from the chemical composition of a melt (Mills, 1993), however, it parameterises melt structure as it considers the structural role played by each cation (e.g., Mysen et al., 1982). NBO/T does not account for different chemical contributions of cations with the same structural role. The melt chemistry can be parameterised by Λ, which is a measure of the ability of O in a melt to donate electron density to a cation and hence stabilise positive charge. Although NBO/T and Λ are parametrisations that simplify the complexity of melt structure and composition they have been found to correlate with the oxidation state of minor components (Burnham and Berry, 2014; Burnham et al., 2015; Miller et al., 2019). Melts may also be parameterised by their compositional components expressed as wt. %, mole fractions or in various ratios (e.g., Lauer and Morris, 1977; O'Neill and Berry, 2021).

The Λ and single-cation mole fraction compositional models were able to better describe the effect of composition on $Cu^+/\Sigma Cu$ than NBO/T. The Λ model parameterises melt composition with a single variable (C in Eqs. (6), (7) and (8)), whereas the single-cation mole fraction model uses a parameter (c_z) for each oxide. Further, while the Λ_z are general

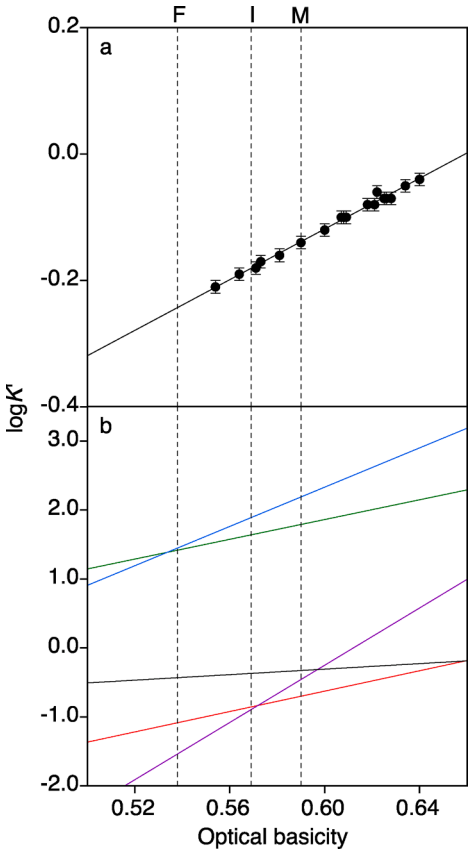

Fig. 4. (a) logK' (symbols; Table 5) at 1300 °C for CNMAS compositions parameterised by optical basicity, and **(b)** the logK' at 1400 °C predicted for Cu^+/Cu^{2+}(black) using Eq. (8) and the parameters determined using the optical basicity model (Table 4), Cr^{2+}/Cr^{3+} (green; Berry et al., 2021), Eu^{2+}/Eu^{3+} (blue; Burnham et al., 2015), Ce^{3+}/Ce^{4+} (red; Burnham and Berry, 2014) and Sb^{3+}/Sb^{5+} (purple; Miller et al., 2019) in CNMAS glasses. The line of best fit to logK' in (a) is shown. The optical basicity of average mafic (M), intermediate (I) and felsic (F) compositions are indicated by the black dashed lines. The reader is referred to the online article for the colour version of this figure.

parameters for any system, the c_z specifically describe the effect of an oxide on the relative stabilities of Cu^+ and Cu^{2+}. The correlation between the c_z and Λ_z of each oxide indicates that the two models are essentially the same, and that melt basicity is the primary compositional control on $Cu^+/\Sigma Cu$. The better correlation between $Cu^+/\Sigma Cu$ and Λ compared to NBO/T is consistent with the results of other redox variable pairs where the degree of melt polymerisation has been observed to exert a weaker control than melt chemistry (e.g., Burnham and Berry, 2014; Burnham et al., 2015; Miller et al., 2019).

The logK' values have a positive correlation with Λ and $\Sigma c_Z X_Z$ (Tables 1, 5; Fig. 4). The positive correlation indicates that melts with large Λ and $\Sigma c_Z X_Z$ preferentially stabilise Cu^{2+}. This is consistent with results of similar studies on the redox ratios of Cr^{2+}/Cr^{3+}, Ce^{3+}/Ce^{4+}, Eu^{2+}/Eu^{3+}, and Sb^{3+}/Sb^{5+}, where intermediate or felsic melts stabilise a larger proportion of the reduced cation under more oxidising conditions than basic melts (Fig. 4). The tendency for basic melts to stabilize an element in its higher oxidation state has been recognized as an empirical rule in silicate melt chemistry, but previous results for Cu^+/Cu^{2+} are inconsistent (Schreiber et al., 1994; Thiemsorn et al., 2008; Kaufmann and Rüssel, 2009). The present results show that basic melts do stabilise Cu^{2+}. The slope of logK' with Λ is 2.0 for Cu^+/Cu^{2+}, 7.2 for Cr^{2+}/Cr^{3+}, 7.4 for Ce^{3+}/Ce^{4+}, 14.3 for Eu^{2+}/Eu^{3+} and 21.0 for Sb^{3+}/Sb^{5+} (Fig. 4). The effect of composition on $Cu^+/\Sigma Cu$ is significantly smaller relative to that of these other redox pairs.

The values of c_z can be compared to those from a similar study on the dependence of Cr^{2+}/Cr^{3+} on composition in CNMAS melts (O'Neill and Berry, 2021). There is a good correlation between the c_z (R = 0.9) but the slope is 2.0(3), reflecting the different sensitivities of Cu^+/Cu^{2+} and Cr^{2+}/Cr^{3+} to melt composition. In the case of Cr, the influence of melt composition can be ascribed to Cr^{3+}, because independent experimental determinations of the activity coefficients of Cr^{2+} as a function of melt composition (O'Neill and Berry, 2006) established that this quantity does not vary sufficiently to account for the compositional dependence (O'Neill and Berry, 2021). In the case of Cu there is no comparable information available to attribute the changes in Cu^+/Cu^{2+} to either Cu^+ or Cu^{2+}, but it is noted that neither cation is expected to have the regular octahedral coordination of Cr^{3+}.

As temperature increases $Cu^+/\Sigma Cu$ increases at a given fO_2, when defined relative to the conventional standard state of O_2 (Fig. 1c; Table 2). The fits predict a linear dependence of logK' on reciprocal temperature (Fig. 5a). The stoichiometry of the redox reactions (i.e., $M^{x+}O_{x/2} + (y\text{-}x)/4O_2 = M^{y+}O_{y/2}$) ensures that the ratio of oxidised to reduced species (M^{y+}/M^{x+}) in silicate melts always decreases with increasing temperature, because the reduced side of the equilibrium includes O_2 (the concentration of which decreases as temperature increases at one atmosphere). In order to reveal the effect of temperature in a way that is more geologically intuitive, the fO_2s of natural systems are often quoted relative to divariant equilibria or 'buffers' such as FMQ. When $Cu^+ = Cu^{2+}$ Eq. (3) can be rearranged to give $\log fO_2 = -4\log K'$, and using logK' values obtained using Eq. (11a) the fO_2 at which $Cu^+/\Sigma Cu = 0.5$ can be determined. The dependence of this fO_2 on temperature is approximately parallel to FMQ (Fig. 5b), which is similar to the behaviour of Fe^{2+}/Fe^{3+} (O'Neill et al., 2018) and Eu^{2+}/Eu^{3+} (Burnham et al., 2015) but different to that of Cr^{3+}/Cr^{2+}.

Melt composition has not been found to have a significant effect on the temperature dependence of Ce^{3+}/Ce^{4+}, Eu^{2+}/Eu^{3+} or Cr^{2+}/Cr^{3+} (Burnham and Berry, 2014; Burnham et al., 2015; Berry et al., 2021), albeit the effect of temperature was only determined for a limited number of CMAS compositions in these studies. The effect of temperature on $Cu^+/\Sigma Cu$ was investigated for two very different compositions; a CMAS melt and a hydrous granite. The ability of the model to fit both compositions well suggests that the effect of temperature on Cu^+/Cu^{2+} is not compositionally dependent, although given the small effect of composition on $Cu^+/\Sigma Cu$ this is unsurprising. Extrapolating the effect of temperature on $Cu^+/\Sigma Cu$ to the temperatures of andesitic (~1000 °C) and granitic (~750 °C) melts would cause a change in $Cu^+/\Sigma Cu$ of<0.005 at $\Delta FMQ = 0$.

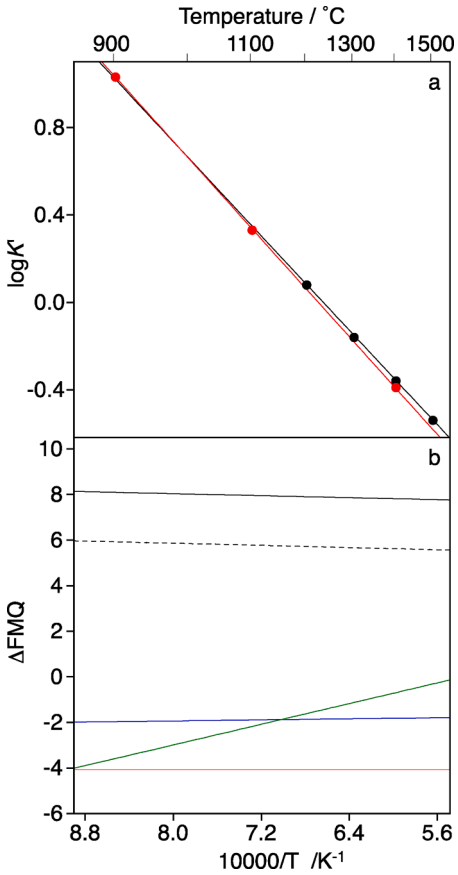

Fig. 5. **(a)** logK' (symbols; Table 6) and the predicted logK' (lines) using Eq. (8) and the parameters determined using the optical basicity model (Table 4), for CMAS7G (black) and hydrous granite (red), and **(b)** the difference in logfO_2 between FMQ and that where $Cu^+/\Sigma Cu = 0.5$ (black) predicted using Eq. (11a), $Fe^{2+}/\Sigma Fe = 0.5$ (red; O'Neill et al., 2018, 2019), $Cr^{2+}/\Sigma Cr = 0.5$ (green; Berry et al., 2021) and $Eu^{2+}/\Sigma Eu = 0.5$ (blue; Burnham et al., 2015), as a function of reciprocal temperature. The uncertainties in (a) are smaller than the size of the symbol. The magnetite – haematite fO_2 buffer is shown by the dashed line in (b). The reader is referred to the online article for the colour version of this figure.

The redox reaction stoichiometry suggests that increasing pressure at constant fO_2 should favour the reduced species, since the partial molar volume of the oxidized component will usually be larger as it contains more oxygens (e.g., the component $Cu^{2+}O$ has twice as many oxygens per Cu atom as $Cu^+O_{0.5}$). This effect may be counteracted by the decrease in size of cations with increasing charge. Adding to the complexity is an increase in coordination environment with increasing pressure exhibited by some cations (e.g., Mare et al., 2021 and references therein). The effect of pressure on $Cu^+/\Sigma Cu$ appears to be compositionally dependent, with increasing pressure having little effect on $Cu^+/\Sigma Cu$ in CMAS7G but preferentially stabilising Cu^+ in the granite composition (Fig. 6). For the granite composition the effect of pressure is consistent with the difference in the partial molar volume of the two species. This indicates that in CMAS melts the effect of the different partial molar volumes of CuO and Cu_2O is compensated for by a strong stabilisation of either Cu^+ or Cu^{2+}. As only two melt compositions were studied as a function of pressure it is difficult to ascertain the cause of the differences. In Fig. 6b the effect of pressure (from 0 to 2.6 GPa), at $\Delta FMQ = 0.1$, on $Cu^+/\Sigma Cu$, $Fe^{3+}/\Sigma Fe$ (Kress and Carmichael, 1991) and $Cr^{2+}/\Sigma Cr$ (Berry et al., 2021) in MORB are shown. Pressure has little effect on $Cu^+/\Sigma Cu$ and $Fe^{2+}/\Sigma Fe$ but a significant effect on $Cr^{2+}/\Sigma Cr$

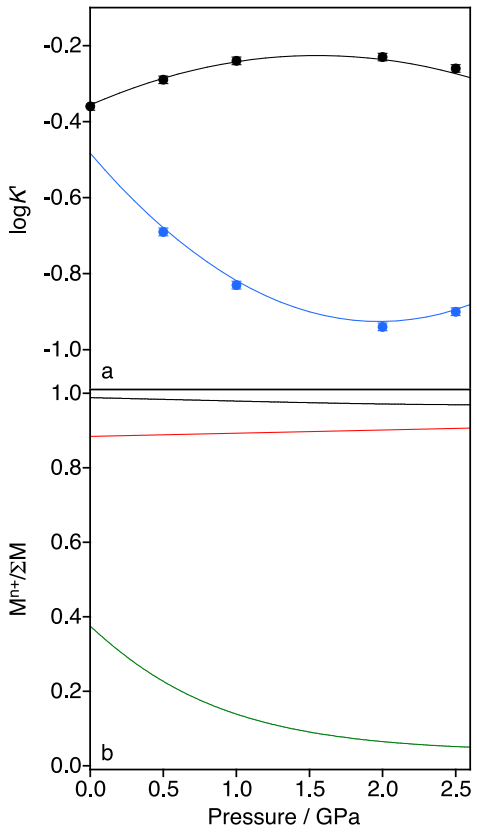

Fig. 6. **(a)** logK' (symbols; Table 6) and the predicted logK' (lines) at 1400 °C using Eq. (8) and the parameters determined using the optical basicity model (Table 4) for CMAS7G (black) and granite (blue), and **(b)** $M^{n+}/\Sigma M$, where M is the redox variable element and n is the reduced oxidation state, as a function of pressure, predicted for $Cu^{+}/\Sigma Cu$ (black; Eq. (11a)), $Fe^{2+}/\Sigma Fe$ (red; Kress and Carmichael 1991) and $Cr^{2+}/\Sigma Cr$ (green; Berry et al., 2021) in MORB at 1400 °C and ΔFMQ = 0.1. The reader is referred to the online article for the colour version of this figure.

(change of ~40% at the fO_2 shown).

$Cu^{+}/\Sigma Cu$ values determined here can be compared to those inferred from the solubility and/or partitioning of Cu between metal and silicate melt. Cu was found to have an average valance state of 1.1(2) in eleven studies of silicate melts equilibrated from 1100 to 1300 °C under reducing conditions (ΔFMQ ≤1.86; see Table 6 in Holzheid and Lodders, 2001). This average is consistent with the results of this study as Equation (11a) predicts $Cu^{+}/\Sigma Cu > 0.99$ under these conditions.

5.2. *The coordination environments of Cu^{+} and Cu^{2+}*

Variations in the energy and intensity of the $1s \rightarrow 4p$ peak have been related to different coordination environments of Cu^{+}; where the energy varies from 8983.6–8984.2, 8983.1–8983.8, and 8984.7–8986.3 eV and the intensity has values of 0.99 ± 0.13, 0.54 ± 0.08, and 0.49 ± 0.11 for $^{[2]}Cu^{+}$, $^{[3]}Cu^{+}$ and $^{[4]}Cu^{+}$, respectively (Kau et al., 1987). The average energy (8984.4 eV; Table 5) and average maximum intensity (1.10; i.e., when $Cu^{+}/\Sigma Cu = 1$; Table 5) of the $1s \rightarrow 4p$ peak in the present study indicate that Cu^{+} has linear coordination and is likely to occur as O-Cu-O complexes.

The intensity of a transition to an empty 4*p* orbital will be higher than the intensity of a transition to a molecular orbital resulting from the mixing of a 4*p*-orbital and an occupied ligand orbital (Kau et al., 1987). In the latter case, the intensity of the transition is determined by the relative contribution of the Cu 4*p*-orbitals. There is a negative correlation between the maximum $I_{1s/4p}$ and Λ of the glasses (R = 0.92; Fig. 7a). This suggests that as the basicity increases the mixing of the 4*p* orbitals with ligand orbitals increases. The maximum intensity of the $1s \rightarrow 4p$ Cu^{+} peak calculated for MORB lies above the trend defined by the CNMAS glasses (Fig. 7a). This difference is consistent with the $I_{1s/4p}$ determined directly from the spectra of the most reduced MORB and CNMAS samples. The maximum $I_{1s/4p}$ of the only other Fe-bearing composition (andesite), however, is not anomalous (Fig. 7a). At this time the reason behind the anomalously intense $1s \rightarrow 4p$ transition of Cu^{+} in MORB is unknown.

The energy separation between the α and β peaks, determined for the samples where $Cu^{+}/\Sigma Cu = 0$ (Table 5), is consistent with Cu^{2+} occupying a distorted octahedral site in the silicate glasses. The energy difference between the α and β peaks has a positive correlation with the Λ of the glasses (R = 0.80; Fig. 7b) and the average difference ~6.0(2) eV is smaller than that of Cu^{2+} in CuO (7.19 eV). This indicates that the distortion of the coordination environment of Cu^{2+} increases with increasing optical basicity yet is smaller than that in CuO.

The coordination environments of Cu^{+} and Cu^{2+} in the glasses may not be the same as those in the melts, since changes in coordination on quenching can be achieved by small geometric translations on length scales less than an interatomic distance. Such translations are somewhat analogous to martensitic transformations in crystals (O'Neill, 2006) and would be expected to proceed very quickly. The linear coordination of Cu^{+} could plausibly be a low entropy configuration produced during

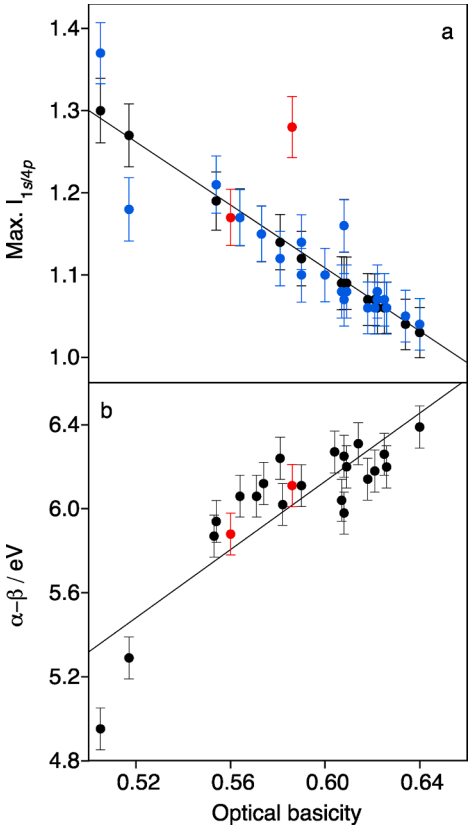

Fig. 7. **(a)** The maximum $I_{1s/4p}$ for Fe-free compositions determined from fitting Eq. (8) to the corrected $I_{1s/4p}$ with composition parametrised by optical basicity (black) and single cation mole fractions (blue), and for Fe-bearing compositions (red; Table 5), and **(b)** the energy separation between the α and β peaks of Cu^{2+} for Fe-free compositions (black) and Fe-bearing compositions (red), versus optical basicity. The lines are the best fits to the data for (a) Max. $I_{1s/4p}$ determined using the single cation mole fraction model and (b) the Fe-free compositions. The reader is referred to the online article for the colour version of this figure.

quenching. However, Cu^{+} has been found to form linear complexes such as Cl-Cu-Cl, O-Cu-Cl, S-Cu-S and O-Cu-S in *in-situ* studies of hydrothermal fluids (Fulton et al., 2000; Berry et al., 2006b; Brugger et al., 2007), suggesting that linear Cu^{+} is stable at high temperatures. Linear O-Cu-O complexes have also been identified in other silicate glass compositions (Maurizio et al., 2000; Bäck et al., 2019), with the only exception being when Cu is associated with S, in which case it is thought to have a distorted trigonal coordination, similar to that in covellite (Lanzirotti et al., 2019).

5.3. Fe-bearing compositions

The oxidation states of two or more redox variable elements in a melt are believed to be independent of each other and only depend on the imposed fO_2 (e.g., Borisov, 2012). The oxidation state of Cu in a melt is given by Eq. (9a), while that of Fe is given by (see Eq. (9a) in O'Neill et al., 2018, 2019):

$$\log\left(Fe^{3+}/Fe^{2+}\right) = 0.25\Delta FMQ - 1.36 + 2.4XCaO \quad (12)$$

where the dependence on temperature is parallel to FMQ and X is the molar fraction calculated on a single-cation basis. For the synthetic MORB composition used here XCaO = 0.14 and substituting this value into Eq. (12), in addition to substituting $\log fO_2$ for ΔFMQ, gives:

$$\log\left(Fe^{3+}/Fe^{2+}\right) = 0.25\log fO_2 + 6262.5/T - 3.18 \quad (13)$$

Subtracting Eq. (13) from Eq. (9a), where the pressure term in Eq. (9a) is 0 as the calculation is at atmospheric pressure and Λ = 0.586 for MORB, eliminates fO_2 and gives:

$$\log\left(Cu^{2+}/Cu^{+}\right) = \log\left(Fe^{3+}/Fe^{2+}\right) - 862.5/T - 0.38 \quad (14)$$

This reformulation of Eq. (9a) allows $Cu^{+}/\Sigma Cu$ to be determined in MORB for a given $Fe^{3+}/\Sigma Fe$.

While the oxidation states of Cu and Fe are independent of each other in a melt, this is not necessarily the case during rapid cooling as the system can no longer equilibrate (exchange O_2) with the imposed fO_2. The $\log K'$ predicted for MORB and andesite using Eq. (8) and the parameters obtained from the Λ model (Table 4) are −0.14 and −0.19, respectively. The $\log K'$ of Fe^{2+}/Fe^{3+} in MORB at 1300 °C is 0.77 (calculated from Berry et al., 2018) and the difference in the $\log K'$ of Cu and Fe suggest that the electron exchange reaction:

$$Cu^{2+}O + Fe^{2+}O = Cu^{+}O_{0.5} + Fe^{3+}O_{1.5} \quad (15)$$

should occur on cooling. The absence of Cu^{2+} in the MORB and andesite samples equilibrated at ΔFMQ ≤ 7.3 suggests that this electron exchange reaction does occur. Cu^{2+} is present in the samples equilibrated at ΔFMQ = 11 as under these conditions Fe^{2+} is essentially absent (Berry et al., 2018).

Substituting $\log K'_{Cu} = \log(Cu^{2+}/Cu^{+}) - 0.25\log fO_2$ and the equivalent expression for Fe^{2+}/Fe^{3+} into Eq. (14), and given that the $\log K'$ of Eq. (15) ($\log K'_{CuFe}$) corresponds to $\log K'_{Fe}$ - $\log K'_{Cu}$, the temperature dependence of the electron exchange reaction for MORB is:

$$\log K'_{CuFe} = 862.5/T + 0.38 \quad (16)$$

The equilibrium constant given by Eq. (16) is >0 for all temperatures and increases with decreasing temperature (Fig. 8a). This indicates that Cu^{+} and Fe^{3+} are always favoured, and increasingly favoured at lower temperatures, relative to Cu^{2+} and Fe^{2+}. The decrease in the number of moles of Cu^{2+}(x) during quenching, which equals the increase in the number of moles of Fe^{3+}, can be calculated at any temperature from the evaluated $\log K'_{CuFe}$ and the initial melt concentrations:

$$K'_{CuFe} = [Cu^{+} + x]\left[Fe^{3+} + x\right] / \left[Cu^{2+} - x\right]\left[Fe^{2+} - x\right] \quad (17)$$

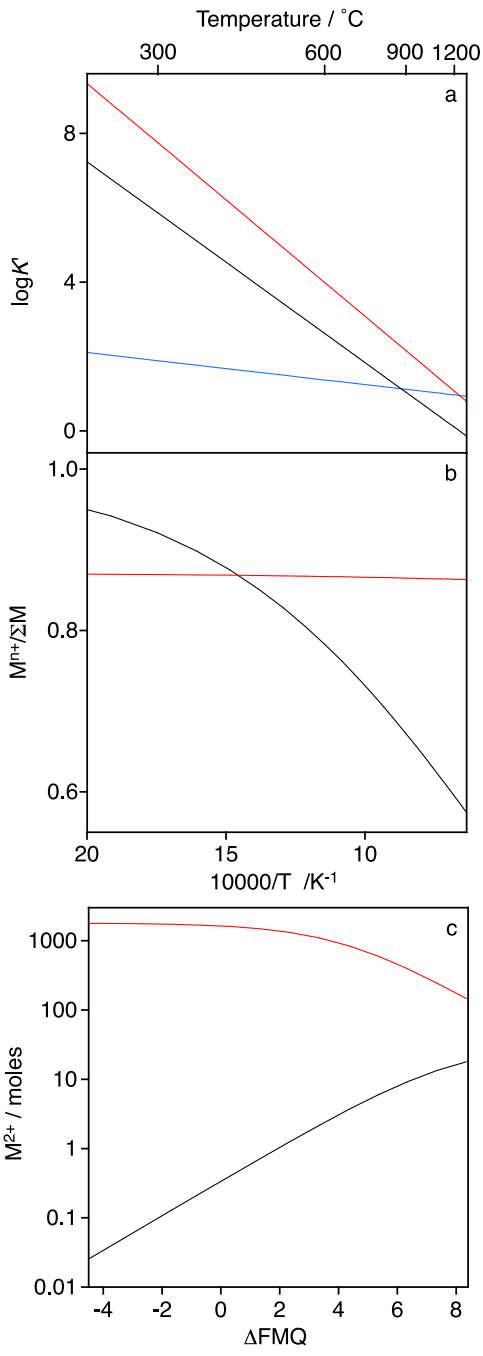

Fig. 8. For a synthetic MORB with 2000 ppm Cu and 10 wt% Fe; **(a)** the temperature dependence of $\log K'_{Cu}$ (black), $\log K'_{Fe}$ (red) and $\log K'_{CuFe}$ (blue), **(b)** the proportion of $Cu^{+}/\Sigma Cu$ (black) and $Fe^{3+}/\Sigma Fe$ (red) after a Fe-Cu electron exchange reaction during quenching from an initial state equilibrated at $\log fO_2 = 0$ and 1300 °C with $Cu^{+}/\Sigma Cu = 0.57$ and $Fe^{3+}/\Sigma Fe = 0.86$, and **(c)** the number of moles of Cu^{2+} (black) and Fe^{2+} (red) in 10^6 g as a function of fO_2. The reader is referred to the online article for the colour version of this figure.

where [] refers to molar concentrations. The increase in Cu^{+} and Fe^{3+} due to an electron exchange reaction was modelled for MORB equilibrated at ΔFMQ = 7.3 and 1300 °C (an initial state of 2000 ppm Cu with $Cu^{+}/\Sigma Cu = 0.57$ and 10 wt% Fe with $Fe^{3+}/\Sigma Fe = 0.86$). The proportion of Cu^{+} increases significantly as the electron exchange reaction becomes more favoured with decreasing temperature (Fig. 8b).

The MORB glass equilibrated at ΔFMQ = 7.3 contains some Cu^{2+} but less than that expected for a Fe free glass. This suggests that an electron

exchange reaction occurred during quenching but that the reaction did not go to completion. An electron exchange reaction between Sb and Fe during quenching was also observed to not reach completion (Miller et al., 2019). As changes in coordination environment mainly occur between the temperature of a melt and that of the glass transition temperature, the Sb and Fe electron exchange was considered to be hindered by the coordination changes required by the changes in oxidation state. This could also be the case for Cu as the coordination change from distorted octahedral for Cu^{2+} to linear for Cu^{+} is large. The spectrum of the MORB glass equilibrated at ΔFMQ = 7.3 suggests $Cu^{+}/\Sigma Cu$ ~0.71, which corresponds to a temperature of 750 °C for the fO_2 imposed at 1300 °C. The glass transition temperature of MORB is 670 °C using the model of Giordano et al. (2008). The similarity of these two temperatures is consistent with the electron exchange reaction for MORB being unable to occur below the glass transition temperature. The absence of Cu^{2+} in the andesite glass equilibrated at ΔFMQ = 7.3 suggests that the electron exchange reaction went to completion. The glass transition temperature of this composition is 740 °C (Giordano et al., 2008). However, the logK' for Fe in this composition is unknown and as the amount of Cu^{2+} removed on cooling will depend on the amount of Fe^{2+} it is unclear how much Cu^{2+} would be expected. For most natural melts the amount of Fe^{2+} will always exceed the amount of Cu^{2+} (Fig. 8c) and hence the magmatic Cu^{+}/Cu^{2+} of a melt is unlikely to be preserved on cooling.

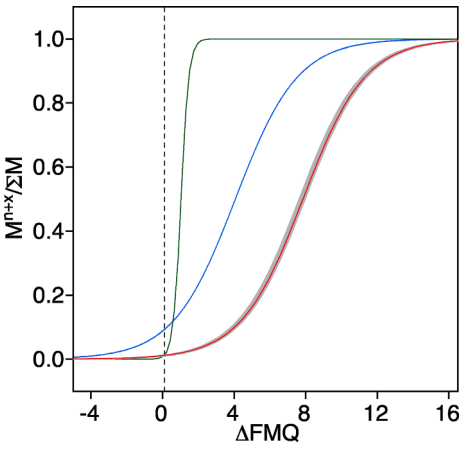

Fig. 9. $M^{n+X}/\Sigma M$, where M is a redox variable element, n is the reduced oxidation state, and x is the stoichiometric number of electrons involved in the redox reaction (x = 1 for Fe and Cu, x = 8 for S), for $Cu^{2+}/\Sigma Cu$ in CNMAS (grey shaded area) and MORB (red) glasses predicted using Eq. (11a), $Fe^{3+}/\Sigma Fe$ (blue; Berry et al., 2018) and $S^{6+}/\Sigma S$ (green; Jugo et al., 2010) as a function of oxygen fugacity relative to FMQ. The average fO_2 of natural MORB (ΔFMQ = 0.1) is shown by the dashed line (Berry et al., 2018). The reader is referred to the online article for the colour version of this figure.

6. Geological implications

Composition has a much weaker effect on Cu^{+}/Cu^{2+} relative to that on Cr^{2+}/Cr^{3+}, Ce^{3+}/Ce^{4+}, Eu^{2+}/Eu^{3+}, and Sb^{3+}/Sb^{5+}(Fig. 4; Berry et al., 2006a; Burnham and Berry, 2014; Burnham et al., 2015; Miller et al., 2019). The linear coordination environment of Cu^{+} is very different to the more highly coordinated environments exhibited by the aforementioned species. The large change in coordination environment from linear (Cu^{+}) to distorted octahedral (Cu^{2+}) necessary for a change in oxidation state could contribute to why Cu^{+}/Cu^{2+} remains effectively constant with changes in composition and melt structure. The relatively low average charge of Cu^{+}/Cu^{2+} could also contribute to the limited sensitivity of Cu^{+}/Cu^{2+} to melt composition. Cu^{+}/Cu^{2+} exhibits a similar temperature dependence to that of Fe^{2+}/Fe^{3+}, Cr^{2+}/Cr^{3+} and Eu^{2+}/Eu^{3+} (Fig. 5a). Given that this is effectively parallel to FMQ temperature will have little effect on Cu^{+}/Cu^{2+} (Fig. 5b). The effect of pressure was found to be compositionally dependent (Fig. 6a), however, changes in $Cu^{+}/\Sigma Cu$ with pressures up to 2.5 GPa are unlikely to be significant (Fig. 6b). The results show that Cu^{+} will be the dominant oxidation state of Cu in crustal and upper mantle silicate melts under terrestrial conditions (Fig. 9).

Mid-ocean ridge melts may transition from parental to more evolved compositions through a process of replenish, tap and fractionation (O'Neill and Jenner, 2012). Fe^{3+} acts as a lightly incompatible element during this process and becomes enriched (O'Neill et al., 2018). The redox state of Fe, as the most abundant redox variable element in basaltic melts, defines the fO_2 of a magma in a closed system and the fO_2 increases from ΔFMQ = −0.31 to 0.36 with melt evolution (MgO changes from 10 to 6 wt.%; Berry et al., 2018; O'Neill et al., 2018). This change in fO_2 corresponds to a barely perceptible change in $Cu^{+}/\Sigma Cu$ from 0.991 to 0.988, such that the proportion of Cu^{2+} remains effectively constant at 1%. The average Cu content of MORB is 86 ppm (Jenner and O'Neill, 2012), of which only ~1 ppm would be present as Cu^{2+}. Cu^{+} is incompatible in all of the silicate minerals and oxides of the upper mantle (Liu et al., 2014; Sun et al., 2020), but is compatible in sulphide liquids (Richards, 2015 and references therein). As sulphide phases are present throughout the differentiation of MORB melts (Jenner, 2017), Cu behaves as a moderately compatible element as MORB evolves.

In convergent-margin (arc) magmatic settings, the variation in fO_2 from approximately ΔFMQ = 0.5 to 3 (Richards, 2015) corresponds to a change in the proportion of Cu as Cu^{2+} from 1 to 4% in basaltic melts and 1 to 2% in andesitic melts (Fig. 9). Thus, Cu^{+} is the dominant oxidation state of Cu in melts associated with Cu porphyry deposits. The proportion of S present as S^{6+} changes from 1% to 99% over the same range in fO_2. This means that sulphide bound Cu^{+} will be released as sulphide converts to sulphate as conditions become more oxidising. The incompatibility of Cu during crystal fractionation under these conditions can lead to a significant enrichment in Cu (Jenner et al., 2010). However, arc magmas may remain sulpide saturated during crustal evolution (Lee et al., 2012; Jenner et al., 2010), while high melt Cu contents are not necessarily required to form Cu porphyry deposits (Blundy et al., 2015). Indeed, rather than form a porphyry deposit Cu in differentiated magmas may be lost to sulphide and silicate cumulates in the lower crust (Jenner, 2017; Lee and Tang, 2020), which if delamination occurs would result in Cu being recycled back into the mantle. The formation of Cu porphyry deposits, rather than being related to anomalously Cu rich melts, is instead related to processes that enable the efficient scavenging of Cu by hydrothermal fluids (Lee and Tang, 2020; Blundy et al., 2015). The speciation of Cu in the silicate melt and exsolving fluid exerts a significant control on the partitioning of Cu between these phases (Berry et al., 2006b; 2009; Lanzirotti et al., 2019). As Cu^{+} is present in both the silicate melts and magmatic fluids (Berry et al., 2006b; 2009) integral to the formation of Cu porphyry deposits, there is no redox control on Cu fluid-melt partitioning and the formation of deposits.

Declaration of Competing Interest

The authors declare that they have no known competing financial interests or personal relationships that could have appeared to influence the work reported in this paper.

Acknowledgements

Dean Scott and David Clark are thanked for their help with sample preparation and Antony Burnham for assistance with Raman spectroscopy and one of the XANES experiments. Part of this research was undertaken at the XAS beamline of the Australian Synchrotron, which is part of ANSTO. Part of this work was performed at GeoSoilEnviroCARS (The University of Chicago, Sector 13), Advanced Photon Source (APS),

Argonne National Laboratory. GeoSoilEnviroCARS is supported by the National Science Foundation – Earth Sciences (EAR-1634415) and Department of Energy (DOE; DE-FG02-94ER14466). This research used resources of the Advanced Photon Source, a U.S. DOE Office of Science User Facility operated for the DOE Office of Science by Argonne National Laboratory under Contract No. DE-AC02-06CH11357. LAM thanks the Australian National University for the award of an International Student PhD scholarship. We thank three reviewers for their comments on the manuscript and Sung Keun Lee for editorial handling.

Appendix A. Supplementary material

An excel spreadsheet showing how NBO/T, optical basicity and single-cation mole fractions are calculated is provided as supplementary material. The input data and python code for fitting Eq. (5) to the corrected $I_{1s/4p}$ with a_0, a_1 and logK' defined by Eqs. (6), (7), and (8), respectively, and melt composition parameterised by either NBOT/T, Λ, or single-cation mole fractions are also provided. Supplementary material to this article can be found online at https://doi.org/10.1016/j.gca.2023.07.021.

References

Alcacio, T.E., Hesterberg, D., Chou, J.W., Martin, J.D., Beauchemin, S., Sayers, D.E., 2001. Molecular scale characteristics of Cu(II) bonding in goethite–humate complexes. Geochim. Cosmochim. Acta 65, 1355–1366.
Bäck, L.G., Sharafat, A., Karlsson, S., Wondraczek, L., Jonson, B., 2019. X-ray and UV-Vis-NIR absorption spectroscopy studies of the Cu(I) and Cu(II) coordination environments in mixed alkali-lime-silicate glasses. J. Non Cryst. Solids 3, 100029.
Ballhaus, C., Berry, R.F., Green, D.H., 1991. High pressure experimental calibration of the olivine-orthopyroxene-spinel oxygen geobarometer: implications for the oxidation state of the upper mantle. Contrib. Mineral. Petrol. 107, 27–40.
Belonoshko, A.B., Saxena, S.K., 1991. A unified equation of state for fluids of CHONS-Ar composition and their mixtures up to very high temperatures and pressures. Geochim. Cosmochim. Acta 56, 3611–3626.
Berry, A.J., O'Neill, H.St.C., Jayasuriya, K.D., Campbell, S.J., Foran, G.J., 2003a. XANES calibrations for the oxidation state of iron in a silicate glass. Am. Min. 88, 967–977.
Berry, A.J., Shelley, J.M.G., Foran, G.J., O'Neill, H.St.C., Scott, D.R., 2003b. A furnace design for XANES spectroscopy of silicate melts under controlled oxygen fugacities and temperatures to 1773 K. J. Synchrotron Radiat. 10, 332–336.
Berry, A.J., O'Neill, H.St.C., Scott, D.R., Foran, G.J., Shelley, J.M.G., 2006a. The effect of composition on Cr^{2+}/Cr^{3+} in silicate melts. Am. Min. 91, 1901–1908.
Berry, A.J., Hack, A.C., Mavrogenes, J.A., Newville, M., Sutton, S.R., 2006b. A XANES study of Cu speciation in high-temperature brines using synthetic fluid inclusions. Am. Min. 91, 1773–1782.
Berry, A.J., Harris, A.C., Kamenetsky, V.S., Newville, M., Sutton, S.R., 2009. The speciation of copper in natural fluid inclusions at temperatures up to 700 °C. Chem. Geol. 259, 2–7.
Berry, A.J., O'Neill, H.St.C., 2004. A XANES determination of the oxidation state of chromium in silicate glasses. Am. Min. 89, 790–798.
Berry, A.J., Stewart, G.A., O'Neill, H.St.C., Mallmann, G., Mosselmans, J.F.W., 2018. A re-assessment of the oxidation state of iron in MORB glasses. Earth Planet. Sci. Lett. 483, 114–123.
Berry, A.J., O'Neill, H.St.C., Foran, G.J., 2021. The effect of temperature and pressure on the oxidation state of chromium in silicate melts. Contrib. Mineral. Petrol. 176, 40.
Blair, R.A., Goddard, W.A., 1980. Ab initio studies of the x-ray absorption edge in copper complexes. I. Atomic Cu^{2+} and $Cu(II)Cl_2$. Phys. Rev. B 22, 2767–2776.
Blundy, J., Mavrogenes, J., Tattitch, B., Sparks, S., Gilmer, A., 2015. Generation of porphyry copper deposits by gas–brine reaction in volcanic arcs. Nat. Geosci. 8, 235–240.
Borisov, A.A., 2012. The Ti4+/Ti3+ ratio of magmatic melts: application to the problem of the reduction of lunar basalts. Petrol 20, 391–398.
Brugger, J., Etschmann, B., Liu, W., Testemale, D., Hazemann, J.L., Emerich, H., Van Beek, W., Proux, O., 2007. An XAS study of the structure and thermodynamics of Cu (I) chloride complexes in brines up to high temperature (400 °C, 600 bar). Geochim. Cosmochim. Acta 71, 4920–4941.
Burnham, A.D., Berry, A.J., 2014. The effect of oxygen fugacity, melt composition, temperature and pressure on the oxidation state of cerium in silicate melts. Chem. Geol. 366, 52–60.
Burnham, A.D., Berry, A.J., Halse, H.R., Schofield, P.F., Cibin, G., Mosselmans, J.F.W., 2015. The oxidation state of europium in silicate melts as a function of oxygen fugacity, composition and temperature. Chem. Geol. 411, 248–259.
Chabiron, A., Pironon, J., Massare, D., 2004. Characterisation of water in synthetic rhyolitic glasses and natural melt inclusions by Raman spectroscopy. Contrib. Miner. Petrol. 146, 485–492.
Chen, J., Mallmann, G., Zhukova, I., O'Neill, H.St.C., 2020. Development of PGE-bearing silicate glass standards for quantitative trace element analysis in silicate-based metallurgical slags. J. Sustain. Metall. 6, 691–699.
Duffy, J.A., 1993. A review of optical basicity and its applications to oxidic systems. Geochim. Cosmochim. Acta 57, 3961–3970.
Ertel, W., O'Neill, H.St.C., Sylvester, P.J., Dingwell, D.B., 1999. Solubilities of Pt and Rh in a haplobasaltic silicate melt at 1300 °C. Geochim. Cosmochim. Acta 63, 2439–2449.
Fortenfant, S.S., Günther, D., Dingwell, D.B., Rubie, D.C., 2003. Temperature dependence of Pt and Rh solubilities in a haplobasaltic melt. Geochim. Cosmochim. Acta 67, 123–131.
Fulton, J.L., Hoffmann, M.M., Darab, J.G., Palmer, B.J., Stern, E.A., 2000. Copper (I) and copper (II) coordination structure under hydrothermal conditions at 325 °C: an X-ray absorption fine structure and molecular dynamics study. J. Phys. Chem. A. 104, 11651–11663.
Giordano, D., Russel, J.K., Dingwell, D.B., 2008. Viscosity of magmatic liquids: A model. Earth Planet. Sci. Lett. 271, 123–134.
Haughton, D.R., Roeder, P.L., Skinner, B.J., 1974. Solubility of sulfur in mafic magmas. Econ. Geol. 69, 451–467.
Holland, T.I.M., Powell, R., 2001. Calculation of phase relations involving haplogranitic melts using an internally consistent thermodynamic dataset. J. Petrol. 42, 673–683.
Holtz, F., Pichavant, M., Barbey, P., Johannes, W., 1992. Effects of H_2O on liquidus phase relations in the haplogranite system at 2 and 5 kbar. Am. Min. 77, 1223–1241.
Holzheid, A., Lodders, K., 2001. Solubility of copper in silicate melts as function of oxygen and sulfur fugacities, temperature, and silicate composition. Geochim. Cosmochim. Acta 65, 1933–1951.
Jenner, F.E., 2017. Cumulate causes for the low contents of sulfide-loving elements in the continental crust. Nat. Geosci. 10, 524–529.
Jenner, F.E., O'Neill, H.St.C., Arculus, R.J., Mavrogenes, J.A., 2010. The magnetite crisis in the evolution of arc-related magmas and the initial concentration of Au, Ag and Cu. J. Petrol. 51, 2445–2464.
Jenner, F.E., O'Neill, H.St.C., 2012. Analysis of 60 elements in 616 ocean floor basaltic glasses. Geochem. Geophys. 13, GC003890.
Jugo, P.J., Wilke, M., Botcharnikov, R.E., 2010. Sulfur K-edge XANES analysis of natural and synthetic basaltic glasses: Implications for S speciation and S content as function of oxygen fugacity. Geochim. et Cosmochim. Acta. 74, 5926–5938.
Kau, L.S., Spira-Solomon, D.J., Penner-Hahn, J.E., Hodgson, K.O., Solomon, E.I., 1987. X-ray absorption edge determination of the oxidation state and coordination number of copper. Application to the type 3 site in Rhus vernicifera laccase and its reaction with oxygen. J. Am. Chem. Soc. 109, 6433–6442.
Kaufmann, J., Rüssel, C., 2009. Thermodynamics of the Cu^{+}/Cu^{2+}-redox equilibrium in soda-silicate and soda-lime-silicate melts. J. Non Cryst. Solids 355, 531–535.
Kiseeva, E.S., Wood, B.J., 2013. A simple model for chalcophile element partitioning between sulphide and silicate liquids with geochemical applications. Earth and Planet. Sci. Lett. 383, 68–81.
Kiseeva, E.S., Wood, B.J., 2015. The effects of composition and temperature on chalcophile and lithophile element partitioning into magmatic sulphides. Earth and Planet. Sci. Lett. 424, 280–294.
Kraft, S., Stümpel, J., Becker, P., Kuetgens, U., 1996. High resolution X-ray absorption spectroscopy with absolute energy calibration for the determination of absorption edge energies. Rev. Sci. Instrum. 67, 681–687.
Kress, V.C., Carmichael, I.S.E., 1991. The compressibility of silicate liquids containing Fe_2O_3 and the effect of composition, temperature, oxygen fugacity and pressure on their redox states. Contrib. Mineral. Petrol. 108, 82–92.
Lanzirotti, A., Lee, L., Head, E., Sutton, S.R., Newville, M., McCanta, M., Lerner, A.H., Wallace, P.J., 2019. Direct measurements of copper speciation in basaltic glasses: understanding the relative roles of sulfur and oxygen in copper complexation in melts. Geochim. Cosmochim. Acta 267, 164–178.
Lauer, Jr.H.V., Morris, R.V., 1977. Redox equilibria of multivalent ions in silicate glasses. J. Am. Cera. Soc. 60, 443–451.
Le Losq, C., Neuville, D.R., Moretti, R., Roux, J., 2012. Determination of water content in silicate glasses using Raman spectrometry: Implications for the study of explosive volcanism. Am. Min. 97, 779–790.
Lebouteiller, A., Courtine, P., 1998. Improvement of a bulk optical basicity table for oxidic systems. J. Solid State Chem. 137, 94–103.
Lee, C.T.A., Tang, M., 2020. How to make porphyry copper deposits. Earth and Planet. Sci. Lett. 529, 115868.
Lee, C.T.A., Luffi, P., Chin, E.J., Bouchet, R., Dasgupta, R., Morton, D.M., Le Roux, V., Yin, Q.Z., Jin, D., 2012. Copper systematics in arc magmas and implications for crust-mantle differentiation. Science 336, 64–68.
Li, Y., Audetat, A., 2012. Partitioning of V, Mn Co, Ni, Cu, Zn, As, Mo, Ag, Sn, Sb, W, Au, Pb, and Bi between sulfide phases and hydrous basanite melt at upper mantle conditions. Earth Planet. Sci. Lett. 355, 327–340.
Li, Y., Audétat, A., 2015. Effects of temperature, silicate melt composition, and oxygen fugacity on the partitioning of V, Mn Co, Ni, Cu, Zn, As, Mo, Ag, Sn, Sb, W, Au, Pb, and Bi between sulfide phases and silicate melt. Geochim. Cosmochim. Acta 162, 25–45.

Liu, X., Xiong, X., Audétat, A., Li, Y., Song, M., Li, L., Sun, W., Ding, X., 2014. Partitioning of copper between olivine, orthopyroxene, clinopyroxene, spinel, garnet and silicate melts at upper mantle conditions. Geochim. Cosmochim. Acta 125, 1–22.
Mare, E.R., O'Neill, H.St.C., Berry, A.J., Glover, C.J., 2020. The stability of divalent Ge in silicate melts and its geochemical properties. Chem. Geol. 532, 119306.
Matjuschkin, V., Blundy, J.D., Brooker, R.A., 2016. The effect of pressure on sulphur speciation in mid- to deep-crustal arc magmas and implications for the formation of porphyry copper deposits. Contrib. Mineral. Petrol. 171, 66.
Maurizio, C., d'Acapito, F., Benfatto, M., Mobilio, S., Cattaruzza, E., Gonella, F., 2000. Local coordination geometry around Cu and Cu ions in silicate glasses: an X-ray absorption near edge structure investigation. Eur. Phys. J. B 14, 211–216.
Miller, L.A., O'Neill, H.St.C., Berry, A.J., Glover, C.J., 2019. The oxidation state and coordination environment of antimony in silicate glasses. Chem. Geol. 524, 283–294.
Mills, K.C., 1993. The influence of structure on the physico-chemical properties of slags. ISIJ International 33, 148–155.
Moretti, R., Ottonello, G., 2003. Polymerisation and disproportionation of iron and sulfur in silicate melts: insights from an optical basicity-based approach. J. Non Cryst. Solids 323, 111–119.
Mysen, B.O., Virgo, D., Seifert, F.A., 1982. The structure of silicate melts: implications for chemical and physical properties of natural magma. Rev. Geophys. Space Phys. 20, 353–383.
Nesbitt, H.W., Bancroft, G.M., Henderson, G.S., 2020. Polymerization during melting of ortho-and meta-silicates: Effects on Q species stability, heats of fusion, and redox state of mid-ocean range basalts (MORBs). Am. Min. 105, 716–726.
O'Neill, H.St.C., 2005. A method for controlling alkali-metal oxide activities in one atmosphere experiments and its application to measuring the relative activity coefficients of $NaO_{0.5}$ in silicate melts. Am. Min. 90, 497–501.
O'Neill, H.St.C., 2006. Free energy of formation of zircon and hafnon. Am. Min. 91, 1134–1141.
O'Neill, H.St.C., Berry, A.J., 2006. Activity coefficients at low dilution of CrO, NiO and CoO in melts in the system CaO-MgO-Al_2O_3-SiO_2 at 1400 °C: Using the thermodynamic behaviour of transition metal oxides in silicate melts to probe their structure. Chem. Geol. 231, 77–89.
O'Neill, H.St.C., Eggins, S., 2002. The effect of melt composition on trace element partitioning: An experimental investigation of the activity coefficients of FeO, NiO, CoO, MoO_2 and MoO_3 in silicate melts. Chem. Geol. 186, 151–181.
O'Neill, H.St.C., Nell, J., 1997. Gibbs free energies of formation of RuO_2, IrO_2 and OsO_2: A high temperature electrochemical and calorimetric study. Geochim. Cosmochim. Acta 61, 5279–5293.
O'Neill, H.St.C., Berry, A.J., McCammon, C.C., Jayasuriya, K.D., Campbell, S.J., Foran, G., 2006. An experimental determination of the effect of pressure on the $Fe^{3+}/\Sigma Fe$ ratio of an anhydrous silicate melt to 3.0 GPa. Am. Min. 91, 404–412.
O'Neill, H.St.C., Jenner, F.E., 2012. The global pattern of trace-element distributions in ocean floor basalts. Nature 491, 698–704.
O'Neill, H.St.C., Berry, A.J., Mallmann, G., 2018. The oxidation state of iron in Mid-Ocean Ridge Basaltic (MORB) glasses: Implications for their petrogenesis and oxygen fugacities. Earth Planet. Sci. Lett. 504, 152–162.
O'Neill, H.St.C., Berry, A.J., Mallmann, G., 2019. Corrigendum to " The oxidation state of iron in Mid-Ocean Ridge Basaltic (MORB) glasses: Implications for their petrogenesis and oxygen fugacities". Earth Planet. Sci. Lett. 527, 115811 [Earth Planet. Sci. Lett. 504 (2018) 152-162].
O'Neill, H.St.C., Berry, A.J., 2021. The oxidation state of chromium in basaltic silicate melts. Geochim. Cosmochim. Acta 306, 304–320.
O'Neill, H.St.C., Pownceby, M.I., 1993. Thermodynamic data from redox reactions at high temperatures. I. An experimental and theoretical assessment of the electrochemical method using stabilized zirconia electrolytes, with revised values for the Fe-"FeO", Co-CoO, Ni-NiO and Cu-Cu_2O oxygen buffers, and new data for the W-WO_2 buffer. Contrib. Mineral. Petrol. 114, 296–314.
Onori, G., Santucci, A., Belli, M., Scafati, A., Della Longa, S., Bianconi, A., Palladino, L., 1988. Cu K-edge XANES of Cu(II) ions in aqueous solution: a measure of the axial ligand distances. Chem. Phys. Lett. 149, 289–294.
Palladino, L., Della Longa, S., Reale, A., Belli, M., Scafati, A., Onori, G., Santucci, A., 1993. X-ray absorption near edge structure (XANES) of Cu(II)–ATP and related compounds in solution: Quantitative determination of the distortion of the Cu site. J. Chem. Phys. 98, 2720–2726.
Paton, C., Hellstrom, J., Paul, B., Woodhead, J., Hergt, J., 2011. Iolite: Freeware for the visualisation and processing of mass spectrometric data. J. Anal. Atom. Spec. 26, 2508–2518.
Pownceby, M.I., O'Neill, H.S.C., 1994. Thermodynamic data from redox reactions at high temperatures. IV. Calibration of the Re-ReO_2 oxygen buffer from EMF and NiO+ Ni-Pd redox sensor measurements. Contrib. Mineral. Petrol. 118, 130–137.
Ravel, B., Newville, M., 2005. ATHENA, ARTEMIS, HEPHAESTUS: data analysis for X-ray absorption spectroscopy using IFEFFIT. J. Synchrotron Radiat. 12, 537–541.
Richards, J.P., 2015. The oxidation state, and sulfur and Cu contents of arc magmas: implications for metallogeny. Lithos 233, 27–45.
Righter, K., Drake, M.J., 2000. Metal/silicate equilibrium in the early Earth - New constraints from the volatile moderately siderophile elements Ga, Cu, P, and Sn. Geochim. Cosmochim. Acta 64, 3581–3597.
Righter, K., Pando, K.M., Danielson, L., Lee, C.T., 2010. Partitioning of Mo, P and other siderophile elements (Cu, Ga, Sn, Ni Co, Cr, Mn, V, and W) between metal and silicate melt as a function of temperature and silicate melt composition. Earth Planet. Sci. Lett. 291, 1–9.
Ripley, E.M., Brophy, J.G., 1995. Solubility of copper in a sulfur-free mafic melt. Geochim. Cosmochim. Acta 59, 5027–5030.
Rudolph, J., Jacob, C.R., 2018. Revisiting the dependence of Cu *K*-edge X-ray absorption spectra on oxidation state and coordination environment. Inorg. Chem. 57, 10591–10607.
Schreiber, H.D., 1987. An electrochemical series of redox couples in silicate melts: a review and applications to geochemistry. J. Geophys. Res. 92, 9225–9232.
Schreiber, H.D., Kochanowski, B.K., Schreiber, C.W., Morgan, A.B., Coolbaugh, M.T., Dunlap, T.G., 1994. Compositional dependence of redox equilibria in sodium silicate glasses. J. Non Cryst. Solids 177, 340–346.
Schreiber, H.D., Wilk Jr, N.R., Schreiber, C.W., 1999. A comprehensive electromotive force series of redox couples in soda–lime–silicate glass. J. Non Cryst. Solids 253, 68–75.
Smith, T.A., Penner-Hahn, J.E., Berding, M.A., Doniach, S., Hodgson, K.O., 1985. Polarized X-ray absorption edge spectroscopy of single-crystal copper(II) complexes. J. Am. Chem. Soc. 107, 5945–5955.
Sossi, P.A., Klemme, S., O'Neill, H.St.C., Berndt, J., Moynier, F., 2019. Evaporation of moderately volatile elements from silicate melts: experiments and theory. Geochim. Cosmochim. Acta 260, 204–231.
Sun, Z., Xiong, X., Wang, J., Liu, X., Li, L., Ruan, M., Zhang, L., Takahashi, E., 2020. Sulfur abundance and heterogeneity in the MORB mantle estimated by copper partitioning and sulfur solubility modelling. Earth and Planet. Sci. Lett. 538, 116169.
Tabelin, C.B., Park, I., Phengsaart, T., Jeon, S., Villacorte-Tabelin, M., Alonzo, D., Yoo, K., Ito, M., Hiroyoshi, N., 2021. Copper and critical metals production from porphyry ores and E-wastes: A review of resource availability, processing/recycling challenges, socio-environmental aspects, and sustainability issues. Resour. Conserv. Recycl. 170, 105610.
Thiemsorn, W., Keowkamnerd, K., Phanichphant, S., Suwannathada, P., Hessenkemper, H., 2008. Influence of glass basicity on redox interactions of iron-manganese-copper ion pairs in soda-lime-silica glass. Glas. Phys. Chem. 34, 19–29.